Old Dominion University Research Foundation

DEPARTMENT OF ENGINEERING TECHNOLOGY
COLLEGE OF ENGINEERING AND TECHNOLOGY
OLD DOMINION UNIVERSITY
NORFOLK, VA 23529

Finite Element Analysis of Reverberation Chambers

By

Charles F. Bunting, Ph.D., Principal Investigator
And
Duc T. Nguyen, Ph.D., Co-Principal Investigator

Final REPORT
For the period ending December 31, 2000

Prepared for the
National Aeronautics and Space Administration
Langley Research Center
Hampton, Virginia 23681

ODURF # 180800
Under
NASA Grant NAG-1-1982
Electromagnetics Research Branch
Flight Electronics Technology Division

December 2000

DEPARTMENT OF ENGINEERING TECHNOLOGY
COLLEGE OF ENGINEERING AND TECHNOLOGY
OLD DOMINION UNIVERSITY
NORFOLK, VA 23529

Finite Element Analysis of Reverberation Chambers

By

Charles F. Bunting, Ph.D., Principal Investigator
And
Duc T. Nguyen, Ph.D., Co-Principal Investigator

Final REPORT
For the period ending December 31, 2000

Prepared for the
National Aeronautics and Space Administration
Langley Research Center
Hampton, Virginia 23681

ODURF # 180800
Under
NASA Grant NAG-1-1982
Electromagnetics Research Branch
Flight Electronics Technology Division

December 2000

Contents

Executive Summary

Finite Element Analysis of Reverberation Chambers

The primary motivating factor behind the initiation of this work was to provide a deterministic means of establishing the validity of the statistical methods that are recommended for the determination of fields that interact in an avionics system. The application of finite element analysis to reverberation chambers is the initial step required to establish a reasonable course of inquiry in this particularly data-intensive study. The use of computational electromagnetics provides a high degree of control of the "experimental" parameters that can be utilized in a simulation of reverberating structures. As the work evolved there were four primary focus areas they are

1. The eigenvalue problem for the source free problem
2. The development of a complex efficient eigensolver
3. The application of a source for the TE and TM fields for statistical characterization
4. The examination of shielding effectiveness in a reverberating environment

One early purpose of this work was to establish the utility of finite element techniques in the development of an extended low frequency statistical model for reverberation phenomena. By employing finite element techniques, structures of arbitrary complexity can be analyzed due to the use of triangular shape functions in the spatial discretization. The effects of both frequency stirring and mechanical stirring are presented. It is suggested that for the low frequency operation the typical tuner size is inadequate to provide a sufficiently random field and that frequency stirring should be used. The results of the finite element analysis of the reverberation chamber illustrate the potential utility of a 2D representation for enhancing the basic statistical characteristics of the chamber when operating in a low frequency regime. The basic field statistics are verified for frequency stirring over a wide range of frequencies. Mechanical stirring is shown to provide an effective frequency deviation. It can be suggested that a large frequency deviation as compared to the operating frequency is required to obtain the desired field statistics. An advantage of employing a numerical scheme such as finite elements to analyze reverberation chambers is that the field values at virtually any point in the structure can be easily obtained without perturbing the field as can occur when using an antenna to monitor the fields.

Essential to the finite element solution of these problems is an effective numerical procedure for solving large-scale, sparse systems of linear equations and generalized eigen-equations. These solution phases typically represent the most costly steps of the analysis in terms of computational resources. Subspace and Lanczos iterations have been developed, well documented, and widely accepted as efficient methods for obtaining p-lowest eigen-pair solutions of large-scale, practical engineering problems. The focus of this work is, however, to re-examine these popular eigen-solution algorithms, with the viewpoints to incorporate recent developments in vectorized sparse technologies in conjunctions with Subspace and Lanczos iterative algorithms for computational electromagnetic enhancements. Basic generalized eigen-solution algorithms are reviewed. Major computational tasks in subspace iteration and Lanczos algorithms have been identified. Efficient sparse technologies have been developed, and fully utilized, in conjunction with the basic Subspace iterations and Lanczos algorithms for efficient solutions of the generalized eigen-equations. Numerical results from practical finite element models have clearly indicated that the proposed "sparse" Subspace iterations and Lanczos algorithms have offered substantial computational advantages over the traditional "skyline", or "variable bandwidth" strategies. Both lumped and consistent mass formulation have been incorporated into our eigen-solution package.

A two-dimensional finite element model for both the transverse electric (TE) and transverse magnetic (TM) solutions inside a simulation reverberation chamber is presented. Tuner effects on the modal structure and the resulting statistics of the field distribution have been explored. It is demonstrated that the TE simulation reverberation chamber provides excellent statistical and reverberation characteristics. The measures of reverberation characteristics includes normalized standard deviation, the max-to-average ratio, the stirrer ratio, and the field uniformity. In addition the notion of "source" stirring is introduced wherein the fields that were coupled into the non-complex geometry were shown to be statistically similar to those in the complex environment. The idea of source stirring may shed light on the question of whether it is absolutely necessary to stir in all regions for which a reverberation type test is being performed. The shielding effectiveness in a reverberating environment was been examined. Coupling shielding effectiveness for TE and TM results was presented. The reverberating environment provides additional insight into the shielding properties in a statistical sense.

Shielding of avionics equipment from both interior and exterior electromagnetic threats is an important part of the system reliability budget. It is typically assumed that the shielding effectiveness of a structure has a level that is a function of frequency for various angles of incidence. Measurements in an anechoic chamber and analysis using computational methods simulate a plane wave environment to quantify shielding effectiveness. An investigation has been performed suggesting that an under certain conditions the aircraft fuselage behaves as a reverberation chamber when stirred internally. Another investigation revealed that the fields in an aircraft flown in the vicinity of a transmitting antenna have levels with characteristics that are statistically similar to a reverberation environment. A conclusion that may be drawn from this is that an aircraft fuselage is a structure in which the interior fields are not plane waves. This significant connection raises an interesting question: What is the shielding effectiveness of an aperture in a reverberating environment? Recently published results for the simulation of the shielding effectiveness of a two-dimensional TM structure in a plane wave environment. Based on the published work, the shielding effectiveness of the TM structure via aperture coupling for several frequencies in a simulated reverberation environment are examined. Measurements were also performed in NASA's reverberation chamber and are presented to provide a connection to the simulated statistical results. A two-dimensional finite element model for transverse magnetic (TM) solution inside a reverberation chamber is presented. Tuner effects on the modal structure and the shielding effectiveness in a reverberating environment are examined. The shielding effectiveness of the TM structure for aperture coupling for several frequencies in a simulated reverberation environment are presented and compared to published and measured results. These results point to the development of a statistical model of shielding effectiveness. This model will form a critical component to the overall mechanism of upset prediction in digital systems.

An Example...

An example of an application of the notion of a probabilistic model for shielding effectiveness a problem of determining the probability of exceeding a particular voltage for a given input voltage. Consider the problem of determining the probability of having an electric field intensity of 1 V/m anywhere inside a cavity exposed at 1000 V/m. The shielding effectiveness has been characterized as a Normal random variable with mean of 35.3 dB and standard deviation of 10.5 dB at a frequency of 400 MHz. The probability of exceeding 1V/m for a 1000 V/m exposure corresponds to calculating the probability of having a shielding effectiveness less than 60 dB which is $F_{SE}(60) = 1 - Q\left(\frac{60 - 35.3}{10.5}\right) = 0.9906$. This calculation predicts a 99.06% probability of exceeding 1V/m for an exposure of 1000 V/m. If the threat level is reduced to 100 V/m the probability of exceeding 1 V/m reduces to 67.36 %.

Chapter 1

A Two Dimensional Finite Element Analysis of Reverberation Chambers

1.1 INTRODUCTION

A reverberation chamber is an enclosure consisting of metal walls with a metallic paddle wheel (denoted a "stirrer" or "tuner") essentially forming a high quality factor (Q) cavity with continuously variable boundary conditions. The fields inside the chamber for a given tuner position are completely deterministic. However, given the nature of the variable boundary condition, the ability of a given source to couple energy into certain modes, and the passband characteristic due the chamber Q, the fields are typically characterized by statistical means. Specifically the probability density functions for the real and imaginary parts of the electric and magnetic fields are normally distributed [1]. In a general three dimensional cavity the field magnitude is χ^2 with six degrees of freedom – the real and imaginary parts of the three field components. A model for the analysis of a two-dimensional cavity consists of an examination of a waveguide structure evaluated at the cutoff frequencies for the modes. Note that at the cutoff frequency the mode exists but does not propagate in a manner similar to the cavity modes. For this study at cutoff the field magnitudes are Rayleigh distributed and the squared fields (related to the power) are exponentially distributed [1] since at most two degrees of freedom exist. The conformity of the actual fields to the specific statistical description is dependent upon the number of modes that can simultaneously exist at a given frequency. The number of modes that can exist at a given frequency is a function of the cavity Q and the operating frequency. Hill [3] gives the two-dimensional specific mode density for finite Q as

$$N_s = \frac{2\pi abf^2}{Qc^2} \tag{1.1}$$

with a and b the dimensions of the structure, f is the operating frequency, c is the velocity of light.

Although the primary methods of characterizing reverberation chambers have been experimental there have been at least two papers which address the numerical analysis of two-dimensional reverberation chambers. The transmission line matrix (TLM) method was employed by Wu [2] to examine the characteristics of the fields in the presence of a large stirrer in a reverberation chamber. Wu used a two-dimensional cavity with a one-dimensional stirrer model to examine the shifting of the eigenfrequencies and the effects on the mode amplitudes for a variety of different stirrer sizes. Wu concludes that the frequency shift for a given stirrer essentially determines the random nature of the fields. Wu also makes an important observation regarding the consequences of the shifting eigenfrequencies in noting that the effect of a large stirrer is essentially a form of random modulation. This modulation is considered to have both amplitude and frequency modulation effects. Wu concludes that an ineffective (electrically small) stirrer is unable to provide adequate frequency modulation effects. Hill [3] examined the concept of electronic mode stirring initially suggested by Loughry [4]. Hill employs a Green's function approach to the analysis of an empty two-dimensional rectangular cavity with an electric line source. Electronic mode stirring essentially implies that instead of stirring via mechanical means to obtain a statistical field distribution, the source can be swept over a narrow bandwidth to effect the shift in eigenfrequencies as suggested by Wu [2].

The purpose of this paper is to establish the utility of finite element techniques in the development of an extended low frequency statistical model for reverberation phenomena. By employing finite element techniques, structures of arbitrary complexity can be analyzed due to the use of triangular shape functions in the spatial discretization. The TLM method uses a rectangular grid structure which introduces an error in the discretization of structures which do not lie along a Cartesian coordinate axis. The finite element method for the source free two-dimensional cavity model yields the fields at all discretized points within the geometry as a result of solving an eigenvalue problem. By contrast the TLM method requires a Fourier transform of the data at all points desired in the field representation. Hill's analysis is applicable to an empty structure so that the relationship between mechanical stirring and frequency stirring cannot be readily explored. Both Wu and Hill consider a two-dimensional structure with a source at a sufficiently high frequency to assure random fields and reasonable field homogeneity consistent with an overmoded structure. The field statistics for reverberation chamber are well known for the case when the chamber is clearly overmoded (such as when exciting the chamber at with an operating frequency that is six times higher than the first resonant frequency of the chamber), but are less defined for undermoded low frequency chamber operation.

In the following section the basic finite element scheme will be described. The approach uses edge elements for the transverse field to eliminate spurious solutions. In section 3 the results for a rectangular structure will be examined. The effects of both frequency stirring and mechanical stirring will be presented. It can will be suggested that for the low frequency operation the typical tuner size is inadequate to provide a sufficiently random field and that frequency stirring should be used. The strengths and limitations of the approach will be presented in the conclusion.

1.2 FINITE ELEMENTS FOR THE REVERBERATION CHAMBER [5-7]

A model for the analysis of a two-dimensional cavity in this paper will consist of a waveguide structure evaluated at the cutoff frequencies for the modes. Note that at the cutoff frequency the mode exists but does not propagate. In the two-dimensional model to be used the cutoff frequencies can me made directly analogous to the resonant frequency of the three dimensional structure. One significant distinction is that the cavity can be considered to possess a bandpass response centered at the operating frequency provided that a cavity mode is supported at that frequency. The width of the response in inversely proportional to the quality factor (*Q*) of the structure. In contrast the two-dimensional waveguide structure can be considered to have a high pass response which supports all modes with cutoff frequencies less than the operating frequency. By using a lossless structure it is possible to examine the infinite Q case where only one mode is considered to exist. It is suggested that this model adequately reflects the physical situation for the low frequency reverberation chamber.

For the development of the finite element method Maxwell's curl equations can be considered in a source free, homogeneous, isotropic, time harmonic form (all sources are assumed steady-state with $e^{j\omega t}$ time dependence) as given by

$$\nabla \times \bar{E} = -j\omega\mu\bar{H} \, , \tag{1.2}$$

and $$\nabla \times \bar{H} = j\omega\varepsilon\bar{E} \, . \tag{1.3}$$

Although analytical results are available for a large class of problems for static, quasi-static, and dynamic conditions, numerical methods typically must be applied whenever the geometry does not coincide with a separable coordinate system.

A full-field approach is required when the medium is characterized by higher order modes, hybrid modes such as for a general inhomogeneous media, or a waveguide or cavity with imperfectly conducting walls. Other problems can be expressed in a scalar form when there is a distinct separation between TE and TM modes. In general this approximation cannot be applied and a full vector formulation is required. The solution for the fields inside the reverberation chamber will be required to support hybrid modes in the presence of any metallic discontinuity or an inhomogeneity due to lossy objects. For the finite element approach the electric field in terms of all three vector components is the desired field quantity. A two dimensional representation for the fields may be expanded in terms of the transverse field and the longitudinal field where

$$\bar{E}(x,y,z)=\left[\bar{e}_t(x,y)+\hat{z}e_z(x,y)\right]e^{-\gamma z}. \tag{1.4}$$

Expressing the del operator as $\nabla=\nabla_t+\hat{z}\frac{\partial}{\partial z}$ and setting $\gamma = 0$ for cutoff, it is possible to write two separate equations - one for the transverse part and another for the z component in terms of the cutoff frequency,

$$\nabla_t\times\left(\frac{1}{\mu_r}\nabla_t\times\bar{e}_t\right)-k_c^2\varepsilon_r\bar{e}_t=0, \tag{1.5}$$

$$\nabla_t\bullet\left(\frac{1}{\mu_r}\nabla_t e_z\right)-k_c^2\varepsilon_r e_z=0, \tag{1.6}$$

leading to the following weighted residual form:

$$\iint\frac{1}{\mu_r}(\nabla_t\times\bar{e}_t)\bullet(\nabla_t\times\bar{T}_t)\,ds=k_c^2\varepsilon_r\iint\bar{e}_t\bullet\bar{T}_t\,ds \tag{1.7}$$

and

$$\iint\frac{1}{\mu_r}(\nabla_t e_z)\bullet(\nabla_t T_z)\,ds=k_c^2\varepsilon_r\iint e_z T_z\,ds. \tag{1.8}$$

Where $k_c=2\pi f_c\sqrt{\mu\varepsilon}$ and is the known as the cutoff wavenumber. Setting $\gamma = 0$ in eq. (1.4) has the effect of rendering the general three-dimensional problem into a two-dimensional problem by suppressing the *z*-behavior. These modes do not propagate and are analogous to the excitation frequencies of a two-dimensional cavity.

The transverse components have been discretized using edge elements and the longitudinal component uses node-based Lagrange functions. After integrating and summing over all elements in the domain the following eigenvalue problem of the form $\mathbf{Ax} = \lambda \mathbf{Bx}$ for the cutoff wavenumber is obtained

$$\begin{bmatrix} S_t & 0 \\ 0 & S_z \end{bmatrix} \begin{bmatrix} e_t \\ e_z \end{bmatrix} = k_c^2 \begin{bmatrix} T_t & 0 \\ 0 & T_z \end{bmatrix} \begin{bmatrix} e_t \\ e_z \end{bmatrix}. \tag{1.9}$$

The solution to the matrix eigenvalue problem yields an eigenvalue-eigenvector pair where the eigenvalue represents the cutoff wavenumber, k_c, and thereby the cutoff frequency, f_c, for the corresponding eigenvector. The eigenvector represents the field solution that is supported at frequencies at and above the cutoff frequency. The reader should be aware that by obtaining the solution to an eigenvalue problem it is implied that for a given excitation frequency it is assumed that the corresponding mode will exist. The basic nature of this source free problem is that a mode exists by virtue of applying a frequency above the cutoff frequency. In a structure with a source only those modes that are supported by the source will exist. Additionally, since we are at cutoff the implication is that each mode exists independently. This model corresponds to a cavity with an infinite Q. The following section will present the results of the finite element analysis to the lossless two-dimensional reverberation chamber model.

1.3 RESULTS

This paper will consider the basic two-dimensional geometry as depicted in Figure 1.1. An anti-symmetric tuner may be rotated to provide mechanical mode stirring, however, the primary results of this work examine the use of a frequency stirring approach. A FORTRAN

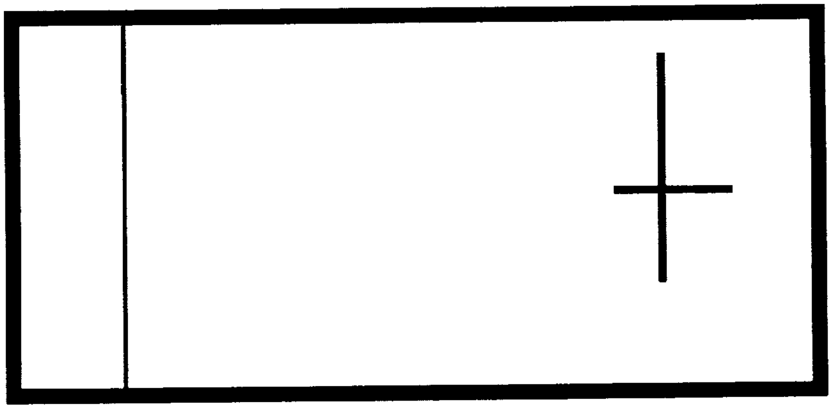

Figure 1.1. Basic 2D Reverberation Chamber.

code applying finite element techniques has been written that provides the electric field at any point within the chamber.

The challenge of applying finite element techniques to reverberation chambers is that enormous computational resources are required. The primary limitation is in the available random access memory (RAM) required for in-core processing. Virtual storage, or out-of-core processing, of the data can also be used, but greatly slows the solution time. Taking advantage of sparsity in the resulting system of equations helps significantly. In spite of the advantages gained by using the sparse eigenvalue solver optimized for the CONVEX the system of equations was limited to the value used in this paper at around 10,000×10,000. (The CONVEX 220 at NASA-Langley has 1 GB of random access memory.) By taking advantage of sparsity the dimensions of the matrices **A** and **B** in eq. (1.9) are reduced to approximately 10,000×7. However, the computation of the eigenvectors results in a full solution matrix whose dimensions are dependent upon the number of eigenvectors desired.

For the reverberation chamber simulation a two-dimensional model of National Aeronautics and Space Administration (NASA) Langley Research Center's B chamber with dimension 3.96 m × 7.10 m was generated and is depicted in Figure 1.2. The resulting system of equations was on the order of 10,000×10,000 and was solved using a CONVEX 220 using a sparse eigenvalue solver in FORTRAN. The data was then processed in MATLAB. The solution of eq. (1.9) has on the order of 10,000 eigenvalues and eigenvectors as possible values of cutoff frequency and corresponding field configurations. Although there are approximately 10,000 solutions available, only those solutions with cutoff frequencies that permit a discretization of 10 samples per wavelength were retained. The rules governing sampling density are not strict and can vary from problem to problem [8] and are related to the Nyquist rate for sampled data. The sampling density has small effect on the accuracy of the cutoff frequency, but has a significant effect on the accuracy of the corresponding field distribution. The level of discretization allowed accurate solutions up to roughly 300 MHz, and resulted in a possible 171 valid cutoff frequencies. A typical result for the field behavior is shown in Figure 1.3 for the *x*-component of the electric field, E_x, at a frequency of 108.1143 MHz. Note that the highest field levels are in the immediate vicinity of the stirrer as would be expected since the fields become infinite near the tuner. Figure 1.4 depicts a higher frequency, 301.069 MHz, for the infinite Q structure and depicts a significantly more complex field structure.

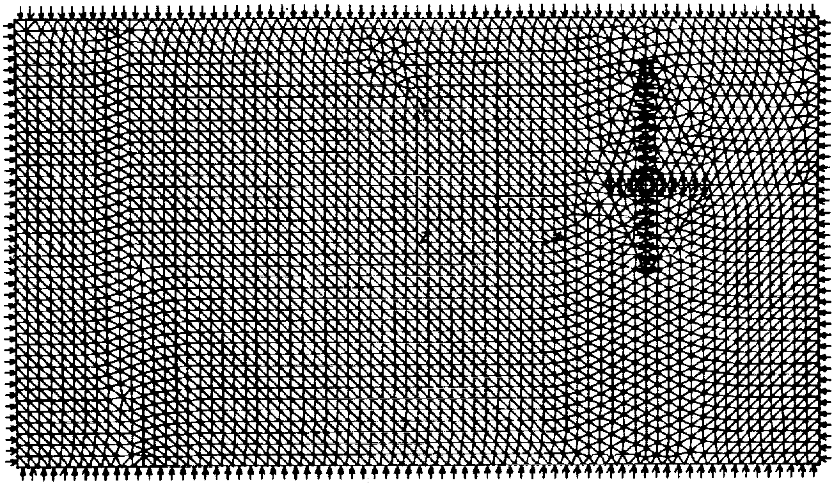

Figure 1.2. Discretization for the two-dimensional geometry.

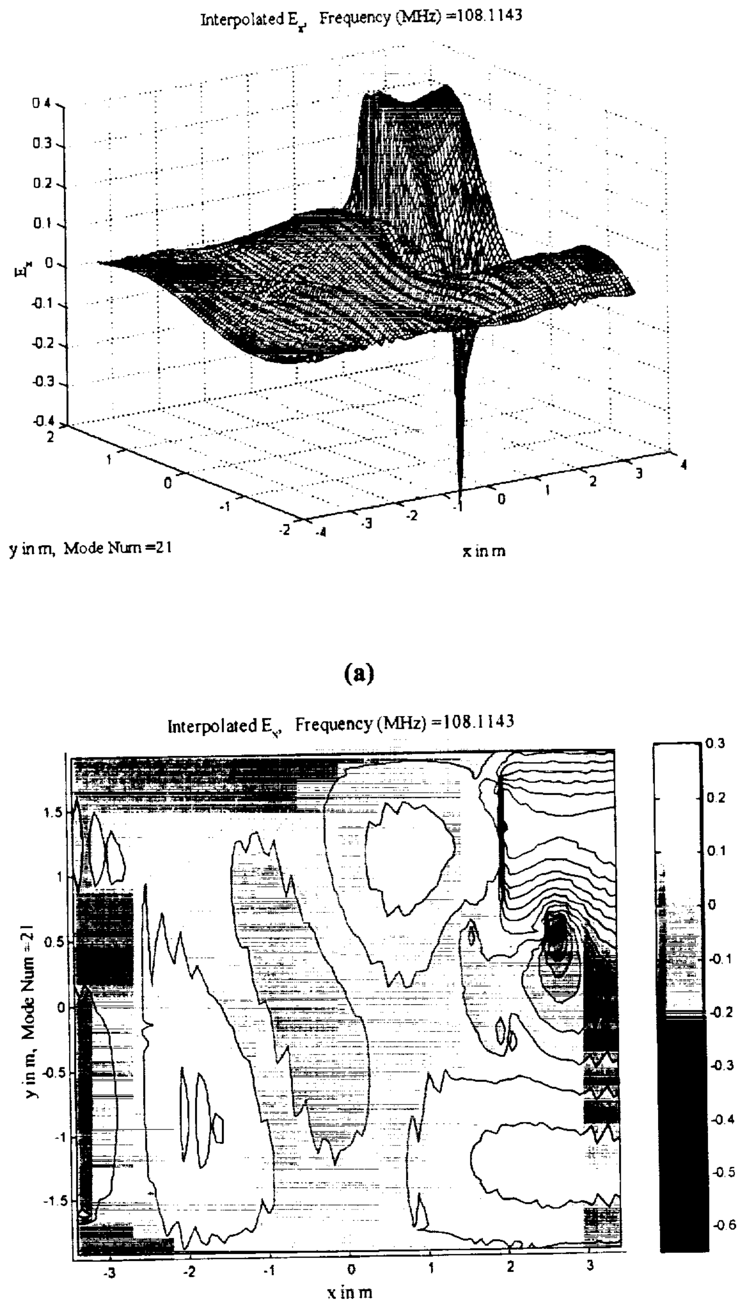

(a)

(b)

Figure 1.3. The *x*-component of the electric field for a frequency of 108.1143 MHz.

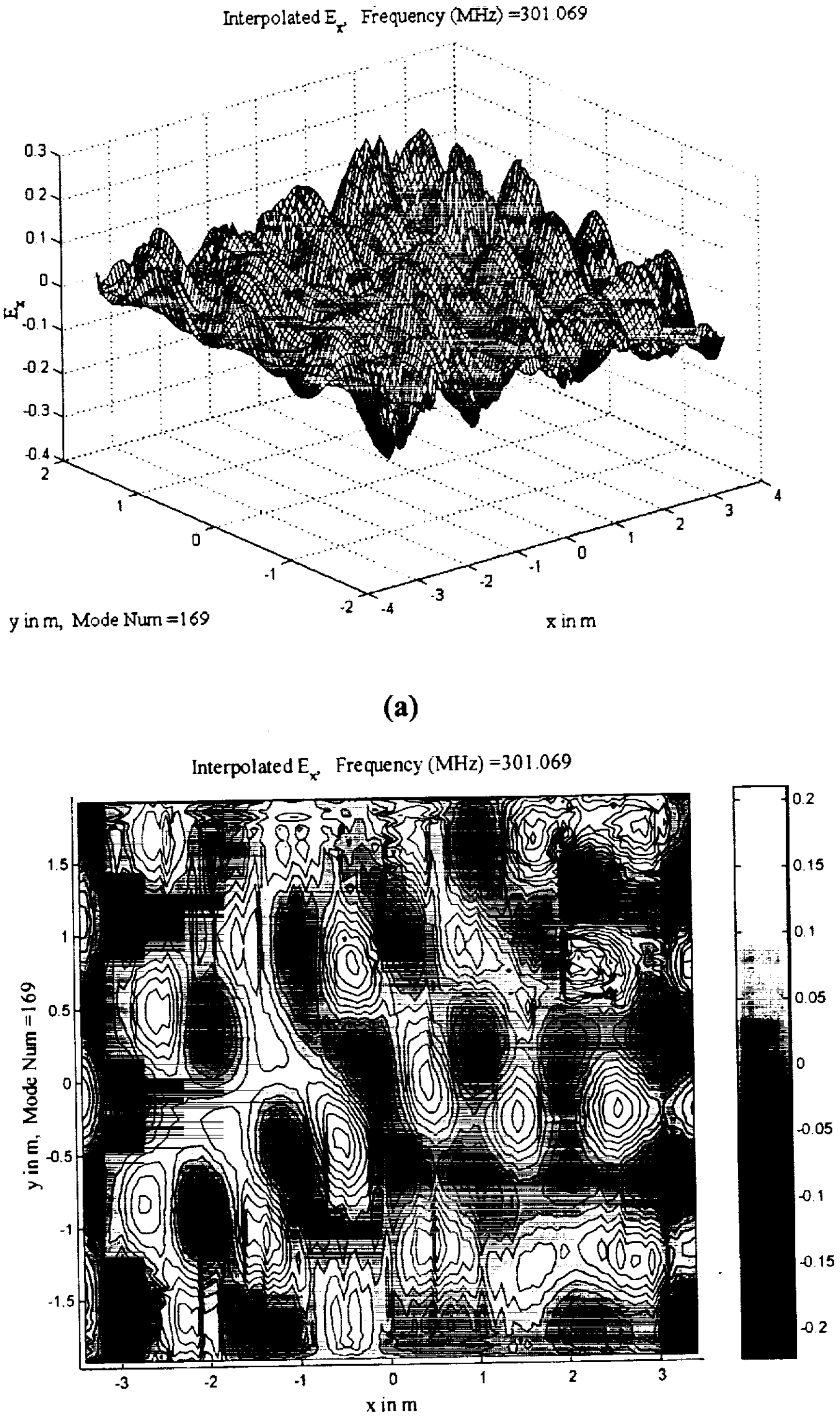

(a)

(b)

Figure 1.4. E_x for 301.069 MHz.

Typical experimental work using a reverberation chamber involves the rotation of the tuner and a measurement of the received power to determine such characteristics as the stirring ratio, or a measurement of the voltage standing wave ratio (VSWR) based on reflected power at the transmit port. The rotation of the tuner provides a variable boundary condition that results in a deterministic variation of the field by applying finite elements. One issue of concern for the eigenvalue problem of eq. (1.9) involving the cutoff frequency is that although all modes are found corresponding to the particular geometrical configuration, the weighting of the modes is not possible. In an actual reverberation chamber the source does not couple energy equally between the possible modes. Another concern is that the modal fields represented by the eigenvectors exist at discrete frequencies and the chamber Q does not directly enter into the formulation. The implication is that the computed modal fields are for an infinite Q chamber, and that multi-moding strictly speaking does not occur since only one mode can exist at a time. We can consider $Q = f_0/B$ for a passband structure with f_0 corresponding to the cutoff frequency f_c. An infinite Q would imply that the bandwidth B would be zero, thus allowing only one mode to exist.

1.3.1 Frequency Stirring

Motivated by the notion that the action of stirring excites the modes weighted by a factor governed by the quality factor of the chamber, and noting that frequency stirring may be used in place of mechanical stirring [3] an interesting experiment was performed. For a fixed tuner position computing all the eigenvalue-eigenvector pairs, within the accuracy constraint based on proper discretization, corresponds to computing all the possible modes that *could be* excited in the chamber. The solutions for cutoff result in a field that is either transverse electric (TE) or transverse magnetic (TM) as the frequency is varied. Consequently, when the solution is TE only E_x and E_y exist and when the solution is TM only E_z exists. Figure 1.5 depicts the amplitude of E_x at one point in the chamber as the frequency is varied. The field variations increase with frequency. This is related to the increased mode density at higher frequencies. A histogram was constructed using MATLAB in Figure 1.6 based on the data of Figure 1.5.

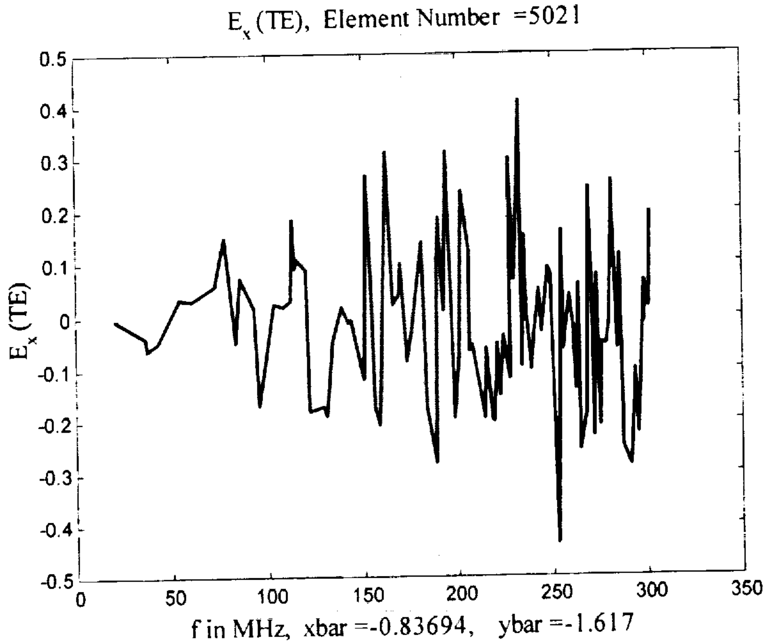

Figure 1.5. The x-component of the electric field for a fixed point inside the chamber as a function of frequency.

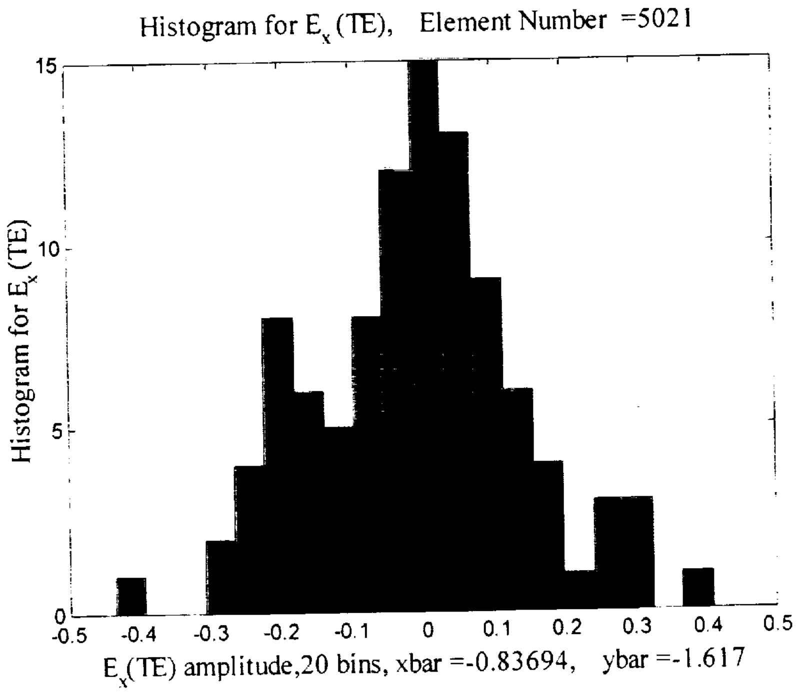

Figure 1.6. The histogram of the data of Figure 1.5.

Any single component should have a Gaussian, or normal distribution [1] with the probability density function, or pdf, given by

$$y = f\left(x \middle| \mu, \sigma\right) = \frac{1}{\sigma\sqrt{2\pi}} e^{\frac{-(x-\mu)^2}{2\sigma^2}}, \tag{1.10}$$

with mean μ and standard deviation σ. The results obtained from the histogram are approximately Gaussian considering the limited number of data points used (101 total points for TE). The histogram provides one means of checking basic trends in the data as compared to a known probability density function, but is limited in its ability to adequately characterize the distribution. A useful visualization tool is the use of a probability plot. The normal probability [9,10] plot essentially renders the cumulative distribution of a normal distribution to that of a straight line as depicted in Figure 1.7 (a) for a set of normally distributed data generated from a random number generator. The data are plotted with "+" symbol. A solid line connects the first and third quartiles of the data corresponding to a robust linear fit of the sample statistics. The linear fit is robust with regard to extremes in the data. The dashed line on the plot represents an extrapolation of the data to the ends of the sample. Data that comes from a normal distribution will appear linear on the plot. If the sample data comes from another distribution the data appear to add curvature in the plot. Consider the curvature in Figure 1.7 (b) for a set of exponentially distributed random data. The curvature in Figure 1.7 (b) clearly demonstrates that the data are not normally distributed. The x-component of the electric field, E_x, is examined by means of a probability plot in Figure 1.8. The linearity observed is sufficient to assert that the E_x is normal for the purposes of applying procedures that assume that E_x is normal, such as combining with other field components to assess the statistics of the squared total field as will be done later. A similar test is performed on the other TE field component E_y in Figure 1.9. For the TM fields E_z is obtained and is validated in Figure 1.10.

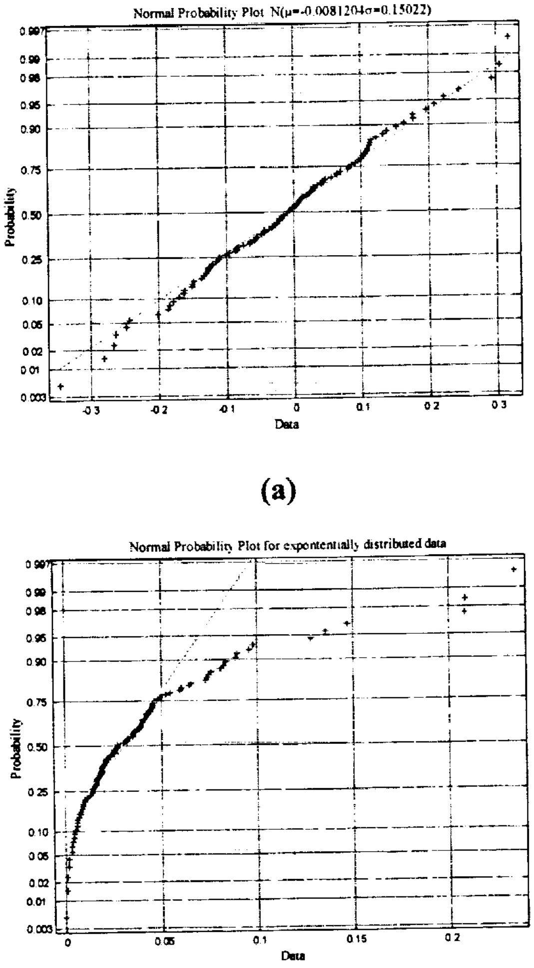

(a)

(b)

Figure 1.7. Normal probability plot from a random number generator for a data count comparable to the data obtainedfor the fields for (a) normal data, and (b) exponentially distributed data.

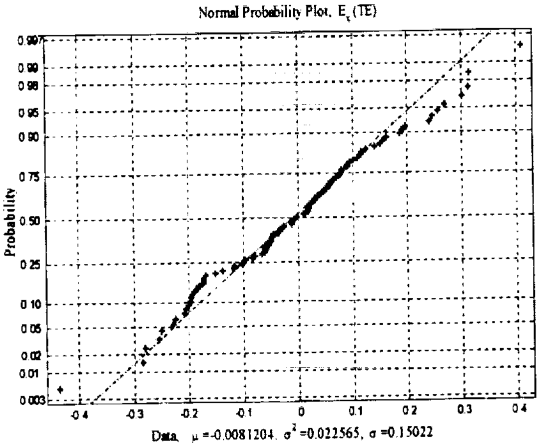

Figure 1.8. Normal probability plot for E_x for a single location as the frequency is varied.

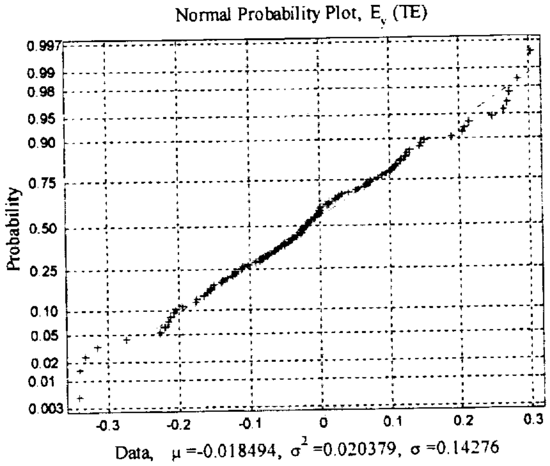

Figure 1.9. Normal probability plot for E_y for a single location as the frequency is varied.

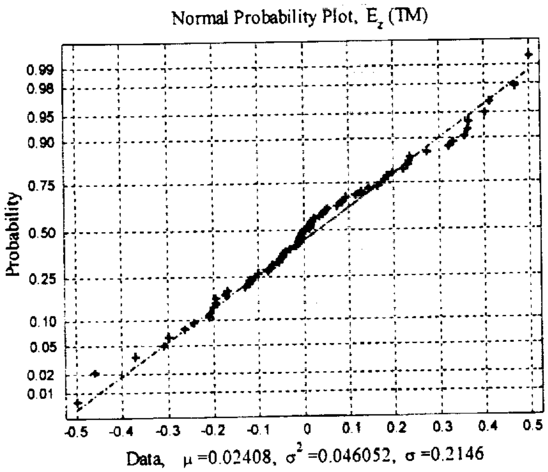

Figure 1.10. Normal probability plot for E_z for a single location as the frequency is varied.

Parameter estimation can be used as a further validation of the underlying statistics by determining the maximum likelihood estimators (MLEs) for data assumed to be taken from a particular distribution. For a normal distribution the MLEs are the mean and standard deviation. The 95 % confidence intervals for the mean and variance are also of interest. The MLEs of a sample set should lie within the confidence interval to assert reasonable agreement of a sample distribution with a known probability density function. The results of the parameter estimation are detailed in Table 1 showing the MLEs and confidence intervals for the data of E_x, E_y, and E_z. The parameter estimation on the field data generated as a result of frequency stirring demonstrates significant agreement within the 95 % confidence interval. The MATLAB Statistical Toolbox was used for the parameter estimation.'

Table 1. Maximum likelihood estimators (MLEs) and 95% confidence intervals.

Normal	μ_{est}	μ_{ci}	σ_{est}	σ_{est}
E_x	-0.00812	(-0.37780,0.02150)	0.15022	(0.13197,0.17436)
E_y	-0.01849	(-0.04668,0.00969)	0.14276	(0.12542,0.16570)
E_z	0.02408	(-0.02709,0.07529)	0.21460	(0.18400,0.25750)
Exponential	a_{est}	a_{ci}	b_{est}	b_{ci}
$E_x^2+E_y^2$	32.381	(25.763,38.998)	1.1870	(-14.523,16.761)

Based on the results of the normal probability plot it can be asserted that both E_x and E_y are normal and can combined as the sum of squared normal data which will result in an exponential distribution. For the TE fields this squared field (proportional to power) data is

$$E_{tot}^2 = E_x^2 + E_y^2 \tag{1.11}$$

The squared field data is depicted in Figure 1.11 with the corresponding histogram in Figure 1.12, and resembles the expected exponential distribution [1].

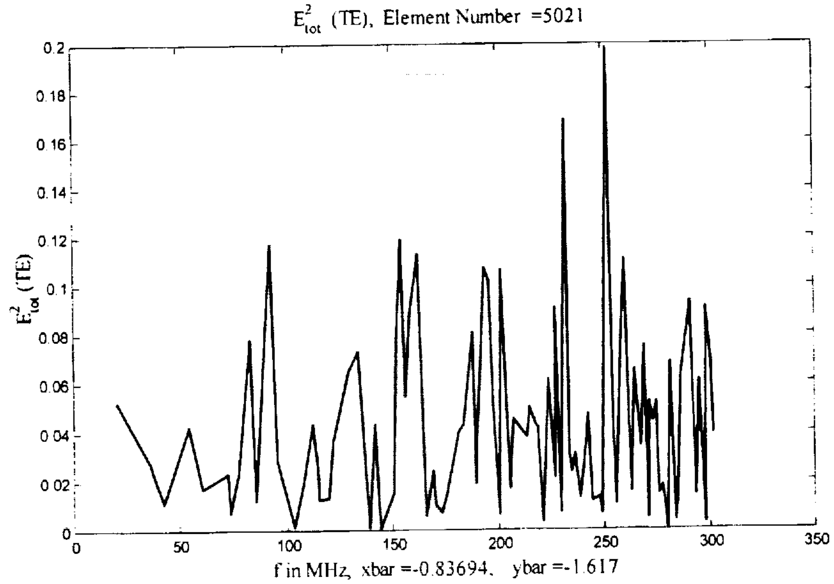

Figure 1.11. The squared field (power) for a single point in the reverberation chamber.

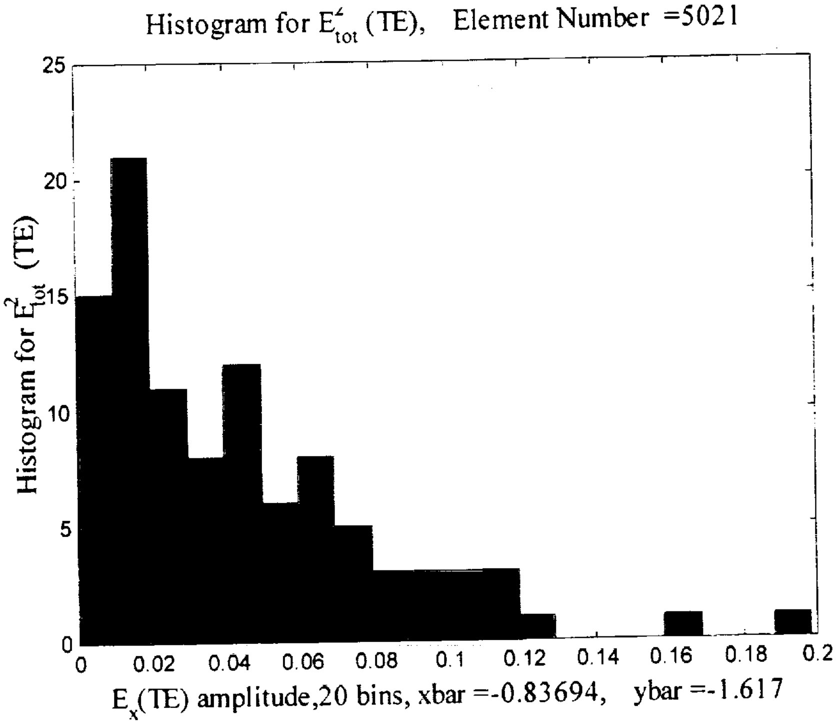

Figure 1.12. The histogram for Figure 1.11.

The probability density function for an exponential distribution is

$$y = f\left(x|\mu\right) = \frac{1}{\mu} e^{-\frac{x}{\mu}} \tag{1.12}$$

with parameter μ. In order to assess the agreement of the total squared field data a Weibull probability plot can used in exactly the same manner as the normal probability plot. The exponential distribution is a special case of a Weibull distribution given by the pdf

$$y = \begin{cases} f\left(x|a,b\right) = abx^{b-1}e^{-ax^b} & ,x > 0 \\ 0 & ,x < 0 \end{cases}. \tag{1.13}$$

The exponential distribution corresponds to $b = 1$ in eq. (1.13). The squared field data are analyzed by means of the Weibull probability plot in Figure 1.13 and demonstrates good agreement. The MLEs for a Weibull distribution are the values of $a_{est} = 32.3807$ and $b_{est} = 1.187$ in eq. (1.13). Of particular significance is the estimator for b which is relatively close to that of the exponential distribution. The 95 % confidence intervals for the estimates are provided in Table 1.

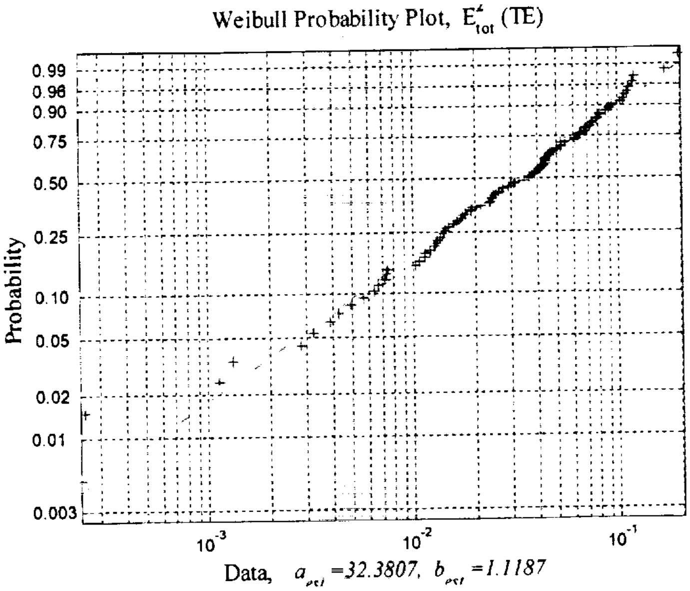

Figure 1.13. Weibull probability plot for the squared fields for a single location as the frequency is varied.

The effects of mode density can be seen in Figure 1.14 for the change in frequency, Δf, versus frequency. Note that the mode density increases as the frequency is increased. One implication of increasing mode density is that additional modes are supported for a fixed non-zero bandwidth giving rise to a multimode environment. For an infinite Q structure the bandwidth is essentially zero so that this implication cannot be readily explored under the current source free environment. Another implication increased mode density is that the field can be significantly altered by exciting alternative modes via changing the cutoff/resonant frequencies of supported modes by changing the physical structure, thus altering the boundary conditions. The changing of boundary conditions is typically accomplished by mechanical stirring and will be discussed in the next subsection.

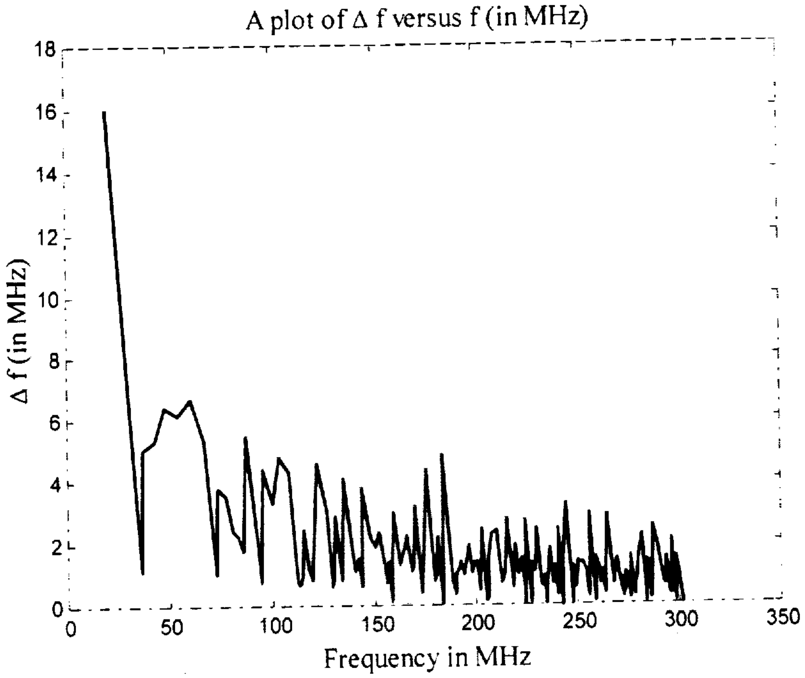

Figure 1.14. A plot of Δ*f* vs. f illustrating the mode density increase as frequency increases.

1.3.2 Mechanical Stirring

The action of mechanical stirring is an important aspect of reverberation chamber analysis. Applying finite elements to a rotating stirrer requires a significant amount of data processing since the field will need to be computed for each tuner position. For the purposes of this investigation the tuner was rotated in 1.6° increments for a total of 225 steps. The increment was chosen to match the step size used by the National Institutes of Science and Technology (NIST) when NASA Langley's chambers were characterized in early 1997. The finite element discretization was reduced to a system size of 3,000 unknowns resulting in an upper frequency limit of 150 MHz. The eigenvalue problem of eq. (1.9) was solved for each position of the tuner which resulted in a total of 43 eigenvalues between the frequencies of 20 MHz and 150 MHz. Figure 1.15 (a) depicts the total field at approximately 60 MHz for three independent points located far from the tuner and greater than half a wavelength from any wall. The total field is periodic and relatively smooth. Figure 1.15 (b) shows similar results for a frequency of approximately 47 MHz.

Work was undertaken to explore various effects of the tuner on the frequency difference between each mode. In this work the assumption of cutoff is advantageous since it is possible to look at each mode in isolation. The first study is the change in frequency versus mode number for a fixed tuner position. The results of Figure 1.16 (a) depict a plot of the frequency difference between the modes for a 1.6° shift in the tuner at a final tuner position of 32 degrees (representing the frequency difference as the tuner is moved from 30.4 to 32 degrees – an arbitrary selection) in part (a). Figure 1.16 (b) depicts the absolute peak frequency deviation for all tuner positions. This study may provide insight into the degree to which a particular mode is affected by the presence of the tuner. One question is: Is there a mode that is more greatly affected by the tuner than another? Another question is: Which mode exhibits the largest maximum frequency deviation? It can be suggested from the data of Figure 1.16 (b) that modes 19 and 20 are most greatly affected by the tuner. The results are suggestive of a means of addressing a long standing question [11] regarding the amount of frequency shift of a given mode that can be obtained by stirrer action to facilitate a comparison to frequency stirring.

The notion of frequency modulation effects [2] suggest a second study to analyze the frequency difference for a particular mode versus tuner position. This second study resulted in the data as presented in Figure 1.17. It can be seen that the modes are significantly affected by the tuner in a complex manner that similar to that of frequency modulation. Figure 1.17 (a) presents the frequency deviation of a single mode as a function of tuner position. Figure 1.17 (b) depicts the absolute peak frequency deviation for all modes versus tuner position. From Figure 1.s 16 and 17 it can be suggested that the tuner exhibits a peak instantaneous frequency deviation of about 1.4 MHz. The random deviation is desired to excite as many modes as possible at a given frequency.

As a third study, animations of the field have been made in which each frame corresponds to the solution for a particular tuner position. These animations provide a means of checking mode continuity for the fields obtained from the matrix of eigenvectors. The modes can shift as the tuner is rotated and it is useful to examine those modes for which a radical departure from a particular mode shape occurs. For some modes the fields rapidly change from

TE to TM as the tuner is rotated. This mode shifting occurs most significantly for modes 19 and 20 as can be inferred from Figure 1.16. This maximum frequency deviation modes 19 and 20 is nearly 1.4 MHz. This large deviation is indicative of mode sensitivity due to the tuner position. It can be suggested that this is a desired condition for proper reverberation chamber operation in a multimode environment. As the cutoff frequency shifts around a particular operating frequency, modes are excited or attenuated (they become evanescent in the two-dimensional structure) and the field variation provides the desired overall field statistics and homogeneity.

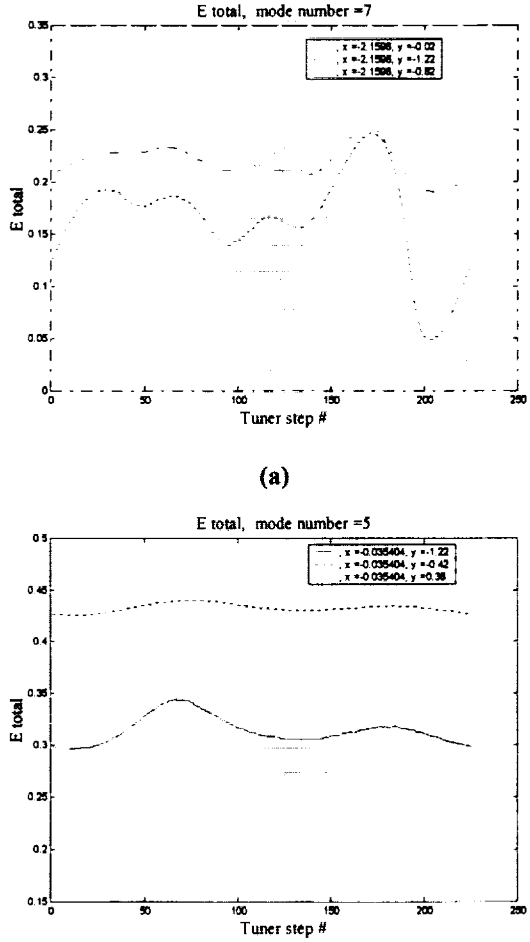

(a)

(b)

Figure 1.15. A plot of the total field for 225 tuner steps at two different points in the chamber. (a) The total field at approximately 60 MHz for three independent points located far from the tuner and greater than half a wavelength from any wall. (b) Similar results at a frequency of approximately 47 MHz.

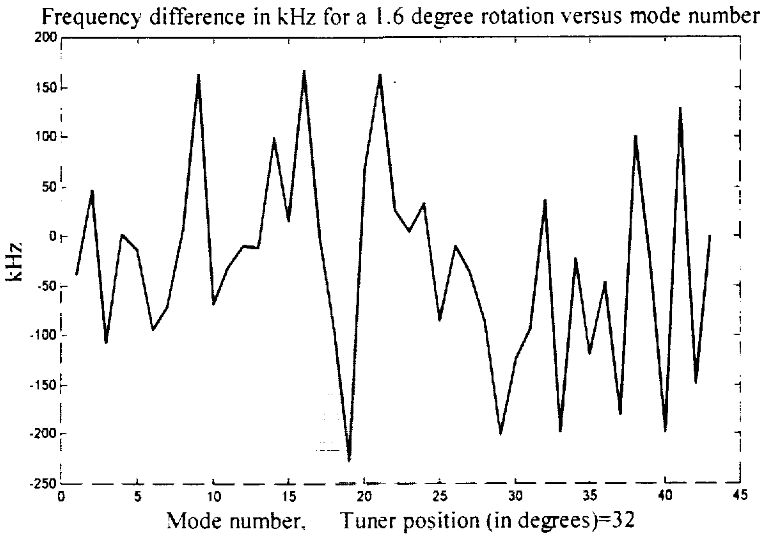

(a)

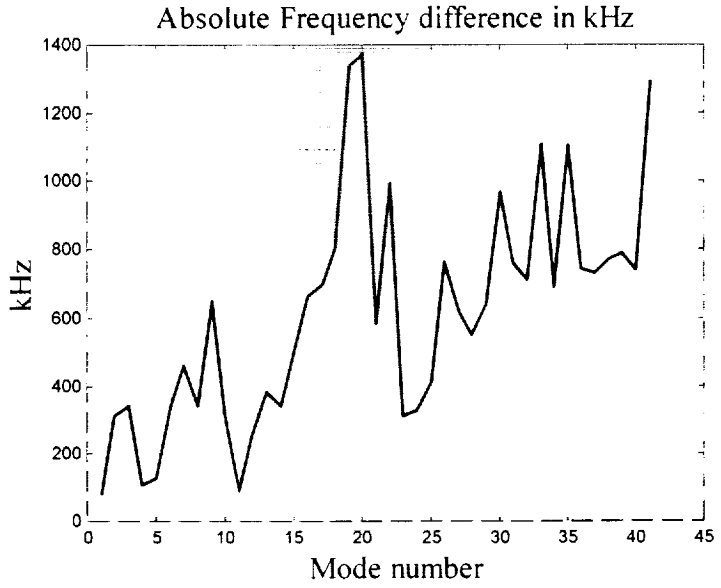

(b) All modes

Figure 1.16. Frequency deviation versus the modes. (a) One tuner position. (b) All tuner positions.

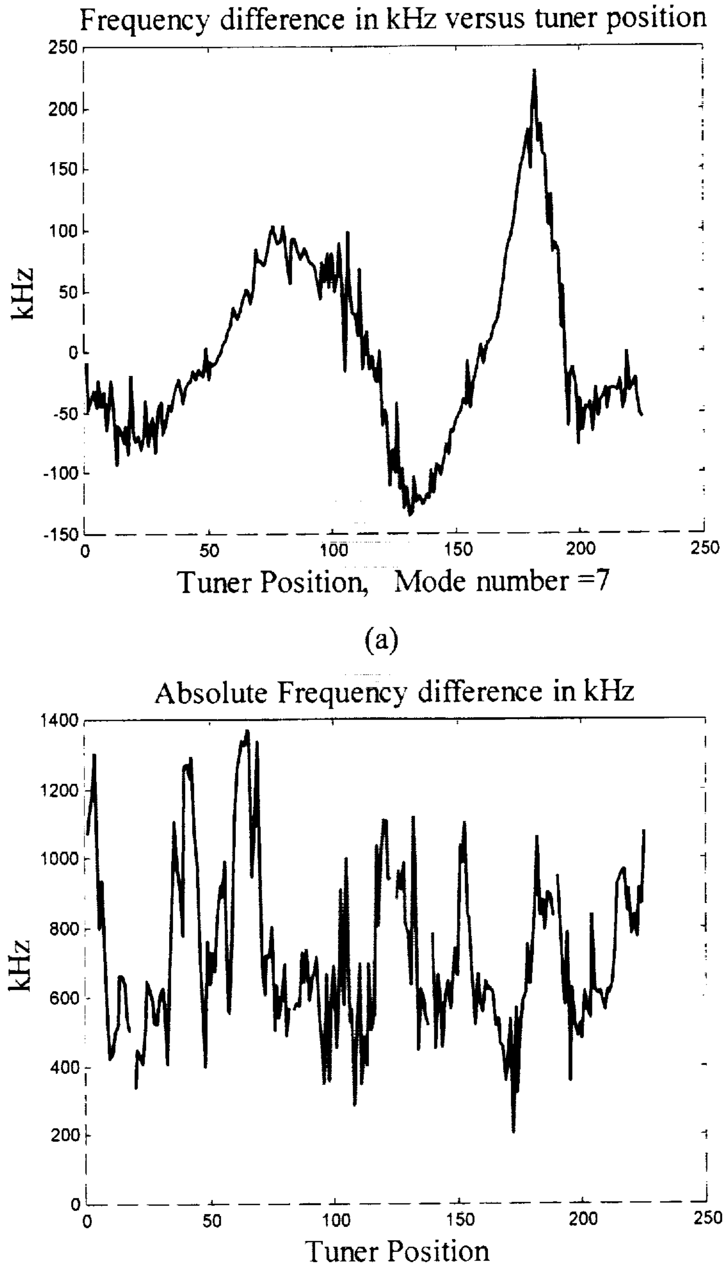

Figure 1.17. Frequency deviation versus tuner position. (a) Single mode (b) All modes.

1.4 CONCLUSIONS AND FUTURE WORK

This paper has presented a two-dimensional analysis of reverberation chambers using finite element techniques. The results of the finite element analysis of the reverberation chamber illustrate the potential utility of a 2D representation for enhancing the basic statistical characteristics of the chamber when operating in a low frequency regime. The basic field statistics are verified for frequency stirring over a wide range of frequencies. Mechanical stirring was shown to provide an effective frequency deviation. It can be suggested that a large frequency deviation as compared to the operating frequency is required to obtain the desired field statistics. The field statistics of mechanical stirring was not specifically explored in this paper since the modes for the cutoff exist in isolation and do not yield desirable characteristics. An advantage of employing a numerical scheme such as finite elements to analyze reverberation chambers is that the field values at virtually any point in the structure can be easily obtained without perturbing the field as can occur when using an antenna to monitor the fields.

Work is continuing in the development of a high speed sparse complex eigensystem solver that will allow the solution of much larger systems (with on the order of 60,000 unknowns) to be analyzed. Other current work includes the coupling of a source to the fields in the 2D geometry by solving the eigenvalue problem for the propagation constant and including a source. The resulting solution would contain the proper mode weighting for the particular configuration depending upon the stirrer position. The author is currently examining the two-dimensional line source problem analogous to Hill's [3] work that addresses low frequency effects on field homogeneity. Future work will also examine the three dimensional problem at low frequencies that include the source.

1.5 REFERENCES

[1] T. H. Lehman, "A statistical theory of electromagnetic fields in complex cavities," *EMP Interaction Notes, No. 494*, 1993.

[2] D.L. Wu and D.C. Chang, "The effect of an electrically large stirrer in a mode-stirred chamber," *IEEE Trans. on Electromag. Compat.*, vol. 31, no. 2, pp. 164-170, 1989.

[3] D.A. Hill, "Electronic mode stirring for reverberation chambers," IEEE Trans. on Electromag. Compat., vol. 36, pp. 294-299, 1994.

[4] T.A. Loughry, "Frequency-stirring: an alternative to mechanical mode-stirring for the conduct of electromagnetic testing," Philipps Laboratory, Kirtland AFB, NM PL-TR-91-1036, Nov. 1991.

[5] C.J. Reddy, M.D. Deshpande, C.R. Cockrell, and F.B. Beck, "Finite element method for eigenvalue problems in electromagnetics," *NASA Technical Paper 3485*, NASA Langely Research Center, Dec. 1994.

[6] J. Jin, *The Finite Element Method in Electromagnetics.* New York: John Wiley and Sons, 1993.

[7] J.L. Volakis, A Chatterjee, and L.C. Kempel, The Finite Element for Electromagnetics: with Applications to Antennas, Microwave Circuits, and Scattering. Piscataway, N.J.: IEEE Press, 1998.

[8] A. C. Cangellaris, "Numerical error in finite element solutions of electromagnetic boundaary value problems," in *Finite Element Software for Microwave Engineering.* Itoh, T. G. Pelosi, and P.P. Silvester, Editors. New York: John Wiley and Sons, 1996.

[9] I. Miller and J. E. Freund, *Probability and Statistics for Engineers, 2nd Edition.* Englewood Cliffs, New Jersey: Prentice Hall, 1977.

[10] The MathWorks, Inc, *Statistics Toolbox: For use with MATLAB, Users Guide, Version 2.* Natick, MA: The Mathworks, Inc., 1997.

[11] D. A. Hill, *Electromagnetic Theory of Reverberation Chambers.* National Institute of Standards and Technology Technical Note 1506, December, 1998.

Chapter 2

Subspace and Lanczos Sparse Eigen-Solvers for Finite Element Structural and Electromagnetic Applications

2.1. INTRODUCTION

The finite element method has been used successfully for the solution of many practical engineering problems in various disciplines, such as structural analysis, fluid mechanics, structural optimization, heat transfer, electromagnetic etc.[1-7]. Essential to the finite element solution of these problems is an effective numerical procedure for solving large-scale, sparse systems of linear equations and generalized eigen-equations. These solution phases typically represent the most costly steps of the analysis in terms of computational resources.

Subspace and Lanczos iterations have been developed, well documented, and widely accepted as efficient methods for obtaining p-lowest eigen-pair solutions of large-scale, practical engineering problems [1,2]. The focus of this paper is, however, to re-examine these 2 popular eigen-solution algorithms, with the viewpoints to incorporate recent developments in vectorized sparse technologies in conjunctions with Subspace and Lanczos iterative algorithms for computational electromagnetic enhancements.

A reverberation chamber (see Figure 1) is an enclosure consisting of metal walls with a metallic paddle wheel (denoted a "stirrer" or "tuner") essentially forming a high quality factor (Q) cavity with continuously variable boundary conditions. The fields inside the chamber for a given tuner position are completely deterministic. However, given the nature of the variable boundary condition, the ability of a given source to couple energy into certain modes, and the passband characteristic due the chamber Q, the fields are typically characterized by statistical means. Specifically the probability density functions for the in-phase and quadrature component of the electric and magnetic fields are normally distributed [8]. The field magnitudes are Rayleigh distributed and the power is exponentially distributed [8]. The degree to which the actual fields conform to the specific statistical description is dependent upon the number of modes that can simultaneously exist at a given frequency is a function of the cavity Q and the operating frequency.

By utilizing a numerical analysis scheme such as finite elements the effects of introducing loss may be accurately simulated, however, for this paper a two-dimensional lossless simulation will be performed.

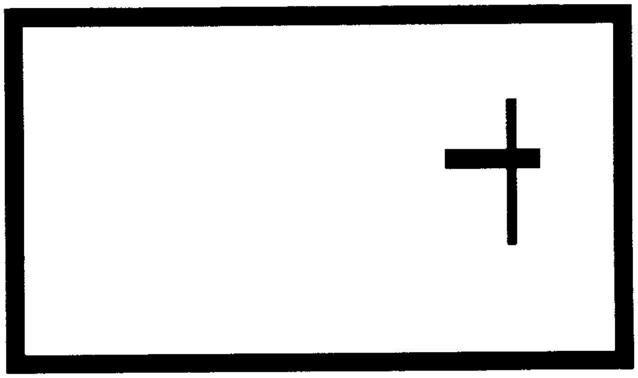

Figure 1. Basic 2D Reverberation Chamber.

A two-dimensional model may yield insight into the nature of the loss experienced on real airframes and also provide an error measure on data in the ideal mode-stirred chamber.

2.2 FINITE ELEMENTS FOR THE REVERBERATION CHAMBER [7]

Consider Maxwell's curl equations in a source free, homogeneous, isotropic, time harmonic form given by

$$\nabla \times \bar{E} = -j\omega\mu\bar{H}, \tag{2.1}$$

$$\nabla \times \bar{H} = j\omega\varepsilon\bar{E}, \tag{2.2}$$

Although analytical results are available for a large class of problems for static, quasi-static, and dynamic conditions, numerical methods typically must be applied whenever the geometry does not coincide with a separable coordinate system.

A full-field approach is required when the medium is characterized by higher order modes, hybrid modes such as for a general inhomogeneous media, or a waveguide or cavity with imperfectly conducting walls. Other problems can be expressed in a scalar form when there is a distinct separation between TE and TM modes. In general this approximation cannot be applied and a full vector formulation is required. The solution for the fields inside the reverberation chamber will be required to support hybrid modes in the presence of any metallic discontinuity or an in homogeneity due lossy objects. For the finite element approach the electric field in terms of all three vector components is the desired field quantity. A two dimensional representation for the fields may be expanded in terms of the transverse field and the longitudinal field where

$$\vec{E}(x,y,z) = \left[\vec{e}_t(x,y) + \hat{z}\, e_z(x,y)\right] e^{-gz} \tag{2.3}$$

Expressing the del operator as $\nabla = \nabla_t + \hat{z}\frac{\partial}{\partial z}$ and setting $\gamma = 0$ for cutoff, it is possible to write two separate equations, one for the transverse part and another for the z component in terms of the cutoff frequency,

$$\nabla_t \mathrm{x}\left(\frac{1}{\mathrm{m}_r}\nabla_t \mathrm{x}\vec{e}_t\right) - k_c^2 \mathrm{e}_r \vec{e}_t = 0 \tag{2.4}$$

$$\nabla_t \bullet \left(\frac{1}{\mathrm{m}_r}\nabla_t e_z\right) - k_c^2 \mathrm{e}_r e_z = 0 \tag{2.5}$$

leading to the following weighted residual form:

$$\iint \frac{1}{\mathrm{m}_r}\left(\nabla_t \mathrm{x}\vec{e}_t\right)\bullet\left(\nabla_t \mathrm{x}\vec{T}_t\right)ds = k_c^2 \mathrm{e}_r \iint \vec{e}_t \bullet \vec{T}_t\, ds \tag{2.6}$$

and

$$\iint \frac{1}{\mathrm{m}_r}\left(\nabla_r e_z\right)\bullet\left(\nabla_t T_z\right)ds = k_c^2 \mathrm{e}_r \iint e_z T_z\, ds \tag{2.7}$$

The transverse components will be discretized using edge elements and the longitudinal component used node-based Lagrange functions. After integrating and summing over all elements in the domain, the following eigenvalue problem of the form **Ax = λ Bx** for the cutoff frequency is obtained

$$\begin{bmatrix} s_t & 0 \\ 0 & s_z \end{bmatrix}\begin{bmatrix} e_t \\ e_z \end{bmatrix} = k_c^2 \begin{bmatrix} T_t & 0 \\ 0 & T_z \end{bmatrix}\begin{bmatrix} e_t \\ e_z \end{bmatrix} \tag{2.8}$$

2.3. BASIC SUBSPACE ITERATION ALGORITHM [1,3]

The generalized eigen-equations (shown in Eq. 2.8), in matrix notation, can be expressed as

$$[K][\phi] = [M][\phi][\lambda] \tag{2.9}$$

In Eq. (9), matrices [K] and [M] represent the structural stiffness and mass, respectively. Matrices $[\lambda]$ and $[\phi]$ represent the eigenvalues and eigenvectors, respectively. The dimension (or degree-of-freedom) of matrices in Eq. (9) is N. For many practical engineering applications, [K] is symmetrical and positive definite. Subspace iteration algorithm can be used effectively to obtain the lowest p eigen-pair solutions. The algorithm can be conveniently described by the following step-by-step procedures as shown in Table 1.

Table 1: Step-by step Basic Subspace Algorithm

Step 1: Select the starting iteration vectors $[Y_1]_{Nxq}$ where $q << N$
Step 2: Factorize the structural stiffness matrix

$$[K] = [L][D][L]^T \tag{2.10}$$

In Eq. (10), [L] is the lower triangular matrix, and [D] is the diagonal matrix

Step 3: For k = 1,2, ... Maxiter, where Maxiter represents the input maximum number of iterations, the following tasks need to be done

Step 4: Solve $[\Phi_{k+1}]_{Nxq}$ from the following matrix equations

$$[K][\Phi_{k+1}]_{N\times q} = [Y_k]_{N\times q} \tag{2.11}$$

Step 5: Compute the reduced stiffness matrix

$$[K^R_{k+1}]_{q\times q} = [\Phi_{k+1}]^T_{q\times N}[Y_k]_{N\times q} \tag{2.12}$$

Step 6: Compute the reduced mass matrix

$$[\bar{Y}_{k+1}]_{N\times q} = [M]_{N\times N}[\Phi_{k+1}]_{N\times q} \tag{2.13}$$

$$[M^R_{k+1}]_{q\times q} = [\Phi]^T_{q\times N}\,[\bar{Y}_{k+1}]_{N\times q} \tag{2.14}$$

Step 7: Solve the reduced eigen-equations

$$[K^R_{k+1}]_{q\times q}[Q_{k+1}]_{q\times q} = [M^R_{k+1}]_{q\times q}[Q_{k+1}]_{q\times q}[\Omega^2_{k+1}]_{q\times q} \tag{2.15}$$

The eigenvalues $[\Omega^2_{k+1}]$ and the associated eigenvectors $[\ Q_{k+1}\ ]$ need to be arranged in the ascending orders (for example $\Omega^2_1 < \Omega^2_2 < \Omega^2_3 < \ldots$)

Step 8: Find an improved approximation to the eigenvectors

$$[Y_{k+1}]_{N\times q} = [\bar{Y}_{k+1}]_{N\times q}[Q_{k+1}]_{q\times q} \tag{2.16}$$

Step 9: Check for convergence. The iterative process will be stopped if either convergence is achieved, or the maximum number of iteration (= Maxiter) is reached (or else, return back to step 3).

2.4. LANCZOS ALGORITHM [1,2]

Recently, the Lanczos algorithm for the solution of generalized eigenvalue problems has been receiving a lot of attention due to its computational efficiency. The original, generalized eigenvalue equation can be written as:

$$K\,\varphi = \omega^2 M\varphi \qquad (2.17)$$

or

$$K_\sigma\varphi = \omega_\sigma^2 M\varphi \qquad (2.18)$$

where K and M are structural stiffness matrix and mass matrix, respectively, $K_\sigma = K - \sigma M$, σ is the shift value and $\omega_\sigma^2 = \omega^2 - \sigma$

Instead of solving Eq. (2.17), or Eq. (2.18) directly, the Lanczos algorithm generates a tri-diagonal matrix T_m

$$T_m = \begin{bmatrix} \alpha_1 & \beta_2 & & & \\ \beta_2 & \alpha_2 & \beta_3 & & \\ & \beta_3 & \alpha_3 & & \\ & & & & \\ & & & & \beta_m \\ & & & \beta_m & \alpha_m \end{bmatrix} \qquad (2.19)$$

through the following three-term recurrence:

$$r_j = \beta_{j-1}q_{j-1} = K_\sigma^{-1}Mq_j - \alpha_j q_j - \beta_j q_{j+1} \qquad (2.20)$$

or in the matrix form:

$$[K_\sigma^{-1}M]Q_m - Q_m T_m = \{0.0....r_m\} = r_m e^T_m \qquad (2.21)$$

$$T_m z = \theta z \qquad (2.22)$$

where $e^T_m = (0,0,...1)$, Q_m is a Nxm orthogonal matrix with columns $q_j = 1,2,3$ ...m, and m is usually much smaller than N. By solving the following reduced eigen system, the eigen solution of Eq. (2.18) can be obtained as

$$\omega_\sigma^2 = \frac{1}{\theta} \tag{2.23}$$

$$\varphi = Q_m z \tag{2.24}$$

For most structural engineering problems, only a few lowest frequencies and the corresponding mode shapes are required, so we have m << N which leads to a significant savings in the number of operations.

A partial restoring orthogonality scheme and a convergence criterion are developed and incorporated into the basic Lanczos algorithm, which is described in a step-by-step procedure, shown in Table 2.

Table 2: Step-by-Step Basic Lanczos Algorithm

Step 1.	Factorization : $K_\sigma = \Lambda \Delta \Lambda^T$
	Form starting vector: $\gamma_o \neq 0$; $\theta_o = 0$
Step 2.	Compute: $M \gamma o$
Step 3.	Compute : $\beta_1 = \sqrt{\gamma_o^T M \gamma_o}$; $q_1 = \frac{\gamma_o}{\beta_1}$
Step 4.	Compute : $\Pi_1 = M\theta_1$
	Lanczos iteration
	For j = 1,2,3, . . . , do
Step 5.	$\epsilon_\varphi = K_\sigma^{-1} \Pi_\varphi$
Step 6.	$\delta_\varphi = \epsilon_\varphi - \beta_\varphi \theta_{\varphi-1}$
Step 7.	$\alpha_\varphi = \theta_\varphi^T M \delta_\varphi = \Pi_\varphi^T \delta_\varphi$
Step 8.	$\gamma_\varphi = \delta_\varphi - \alpha_\varphi \theta_\varphi$
Step 9.	$\Lambda_\varphi = M \gamma_\varphi$
Step 10.	$\beta_{j+1} = (\gamma_j^T M \gamma_j)^{\frac{1}{2}} = \sqrt{\Lambda_j^T \gamma_j}$
	Reorthogonalization of q_{j+1}
Step 11.	$q_{j+1} = \frac{\gamma_j}{\beta_{j+1}}$; $P_{j+1} = \frac{\Lambda_j}{\beta_{j+1}}$
Step 12.	IF necessary solve Eq(14) : $T_\varphi \zeta = \theta \zeta$
	Converged? (If "No", then return to step 5)
Step 13.	Eigenvector transformation: $\phi = \Theta_\varphi \zeta$

2.5. COMPUTATIONAL ENHANCEMENTS FOR SUBSPACE AND LANCZOS ALGORITHMS

It has been pointed out in Sections 2.3-2.4 that matrix factorization, forward & backward equation solution, and matrix-vector (or matrix-matrix) multiplications represent the major computational lasts for Subspace iteration, and Lanczos algorithms. Recent developments in Sparse technologies [3] will be fully utilized to improve the computational efficiency of both Subspace iteration, and Lanczos algorithms.

2.6. BASIC EQUATION SOLUTION ALGORITHMS

The Choleski (or U^TU) factorization is efficient, however, its application is limited to the case where the coefficient stiffness matrix [K] is symmetrical and positive definite. With negligible additional computational efforts, the LDL^T algorithm can be used for broader applications (where the coefficient matrix can be either positive, or negative definite). In this algorithm, the given matrix [K] in Eq. (1) can be factorized as

$$[K] = [L]\,[D]\,[L]^T \tag{2.25}$$

where [L] and [D] are lower triangular matrix (with unit values on the diagonal), and diagonal matrix, respectively. For a simple 3x3 symmetrical stiffness matrix, Eq. (2.25) can be explicitly expressed as

$$\begin{bmatrix} K_{11} & K_{12} & K_{13} \\ K_{21} & K_{22} & K_{23} \\ K_{31} & K_{32} & K_{33} \end{bmatrix} = \begin{bmatrix} 1 & 0 & 0 \\ L_{21} & 1 & 0 \\ L_{31} & L_{32} & 1 \end{bmatrix} \begin{bmatrix} D_1 & 0 & 0 \\ 0 & D_2 & 0 \\ 0 & 0 & D_3 \end{bmatrix} \begin{bmatrix} 1 & L_{21} & L_{31} \\ 0 & 1 & L_{32} \\ 0 & 0 & 1 \end{bmatrix} \tag{2.26}$$

The unknown L_{ij} and D_i can be easily obtained by expressing the equalities between the upper triangular matrix (on the left-hand-side) and its corresponding terms on the right-hand-side of Eq. (2.26).

Since the LDL^T algorithm will be used later on to develop efficient, vectorized sparse algorithm, a pseudo-FORTRAN skeleton code is given in Table 3A (assuming the original given matrix is symmetrical and full).

```
c . . .   Assuming row 1 has been factorized earlier
          DO 11 I =2, N
          DO 22 K =1, I-1
c . . .   Compute the multiplier (Note: U represents L^T)
          XMULT =U(K,I)/U(K,K)
          DO 33 J =I, N
          U (I, J) = U (I, J) - XMULT * U (K, J)
   33     CONTINUE
          U (K, I) = XMULT
   22     CONTINUE
   11     CONTINUE
```

Table 3A: Skeleton FORTRAN Code for LDL^T
(assuming the matrix U is completely full)

2.7. STORAGE SCHEMES FOR THE COEFFICIENT STIFFNESS MATRIX

Successful implementation of a sparse equation solution algorithm depends rather heavily on the reordering method used. While the Reversed Cuthill-Mckee (RCM), or Gipspoole-Stockmyer (GS) . . . reordering algorithms can be used efficiently in conjunction with skyline or variable bandwidth equation solution algorithms [9-10], these reordering algorithms are not suitable for sparse equation solution algorithms. Designing efficient sparse-reordering algorithms is a big task itself, and is outside the scope of this paper. For complete treatments on this subject, the readers are strongly recommended to popular textbooks and articles in the literature [9-10]. In this section, it is assumed that the best available sparse-reordering algorithm, such as Modified Minimum Degree (MMD), or Nested Dissection (ND) [13], has already been applied to the original coefficient matrix [K]. To facilitate the discussions in this section, assuming the resulted matrix [K] (after using MMD, or ND algorithm) takes the following form

$$[K] = \begin{bmatrix} 11. & 0 & 0 & 1. & 0 & 2. \\ & 44. & 0 & 0 & 3. & 0 \\ & & 66. & 0 & 4. & 0 \\ & & & 88. & 5. & 0 \\ SYM & & & & 110. & 7. \\ & & & & & 112. \end{bmatrix} \tag{2.27}$$

In the sparse storage scheme, only non-zero values (and their corresponding locations) of the off-diagonal terms need to be stored. The diagonal terms will be stored in a separated array. For the data shown in Eq. 27 the number of non-zero off diagonal terms (NCOEF) is 6 (thus NCOEF=6).

2.8. SPARSE SYMBOLIC FACTORIZATION

The purpose of symbolic factorization is to find the locations of all nonzero (including "fills-in" terms), off-diagonal terms of the factorized matrix [U] (which has NOT been factorized yet!). Thus, one of the major goals in this phase is to predict the required computer memory for subsequent numerical factorization. The outputs from this symbolic factorization phase will be stored in the following 2 integer arrays (assuming the stiffness matrix data shown in Eq. 2.27 is used):

$$JSTARTROW \begin{pmatrix} 1 \\ 2 \\ 3 \\ 4 \\ 5 \\ 6 \\ 7 = N+1 \end{pmatrix} = \begin{Bmatrix} 1 \\ 3 \\ 4 \\ 5 \\ 7 \\ 8 \\ 8 \end{Bmatrix} \tag{2.28}$$

$$JCOLNUM\begin{pmatrix} 1 \\ 2 \\ 3 \\ 4 \\ 5 \\ 6 \\ 7 = NCOEF2 \end{pmatrix} = \begin{Bmatrix} 4 \\ 6 \\ 5 \\ 5 \\ 5 \\ 6 \\ 6 \end{Bmatrix} \tag{2.29}$$

The following "new" definitions are used in Eqs. (2.28-2.29):

NCOEF2 ≡ The number of nonzero, off-diagonal terms of the factorized matrix [U]

JSTARTROW(i) ≡ Starting location of the first nonzero, off-diagonal term for the i^{th} row of the factorized matrix [U]. The dimension for this integer array is N+1

JCOLNUM(j) ≡ Column numbers associated with each nonzero, off-diagonal terms of [U] (in a row-by-row fashion). The dimension for this integer array is NCOEF2. Due to "fills-in" effects, NCOEF2 > > NCOEF.

2.9 SPARSE NUMERICAL FACTORIZATION

It is generally safe to say that sparse numerical factorization is more complicated for computer coding implementation than its skyline, or variable bandwidth cases. Main difficulties are due to complex "book-keeping" (or index referring) process. The "key" ideas in this numerical phase are still basically quite similar to the operations involved during the symbolic factorization phase. There is an important modification that need to be done on the symbolic factorization, in order to do the sparse numerical factorization (to facilitate the discussion, please refer to the data shown in Eq. 2.27):

> For symbolic factorization purpose, there is no need to have any floating arithmetic calculation. Thus, upon completing the symbolic process for row 4, there are practically no needs to consider row 2 and/or row 3 for possible contributions to row 5. Only row 4 needs to be considered for possible contributions (or "fills-in" effects) to row 5 (since row 4, with its "fills-in", is already full).
>
> For numerical factorization purpose, however, all rows 2, then 4 and then 3 will have to be included in the numerical factorization of row 5.

2.10 SPARSE SOLVER WITH IMPROVED STRATEGIES

To simplify the discussion, assuming that upon completion of the symbolic phase, the stiffness matrix [K] will have the following form

$$[K] = \left[\begin{array}{cccccccccccccc|c}
1 & 2 & 3 & 4 & 5 & 6 & 7 & 8 & 9 & 10 & 11 & 12 & 13 & 14 & \\
x & x & x & & & x & & & x & x & x & & x & x & 1 \\
 & x & x & & & x & & & x & x & x & & x & x & 2 \\
 & & x & & & x & & & x & x & x & & x & x & 3 \\
 & & & x & x & & x & x & & & & & x & & 4 \\
 & & & & x & & x & x & & & & & x & & 5 \\
 & & & & & x & x & x & F & F & F & & x & F & 6 \\
SYM. & & & & & & x & x & x & x & F & & x & x & 7 \\
 & & & & & & & x & x & x & F & & x & x & 8 \\
 & & & & & & & & x & x & F & & x & x & 9 \\
 & & & & & & & & & x & F & & x & x & 10 \\
 & & & & & & & & & & x & x & x & x & 11 \\
 & & & & & & & & & & & x & x & x & 12 \\
 & & & & & & & & & & & & x & x & 13 \\
 & & & & & & & & & & & & & x & 14
\end{array}\right] \qquad (2.30)$$

In Eq. (2.30) the stiffness matrix [K] has 14 dof. The symbols "x" and "F" refer to the original nonzero terms, and the nonzero terms due to "Fills-in", respectively. It can be seen that rows 1-3 have the same nonzero patterns (by referring to the enclosed "rectangular" region, and ignoring the fully populated "triangular" region of rows 1-3). Similarly, rows 4-5 have the same nonzero patterns. Rows 7-10 have the same nonzero patterns. Finally, rows 11-14 also have the same nonzero patterns. Thus, for the data shown in Eq. (2.30), the "Master" (or "Super") dof can be generated as

$$MASTER \begin{pmatrix} 1 \\ 2 \\ 3 \\ 4 \\ 5 \\ 6 \\ 7 \\ 8 \\ 9 \\ 10 \\ 11 \\ 12 \\ 13 \\ 14 = N \end{pmatrix} = \begin{Bmatrix} 3 \\ 0 \\ 0 \\ 2 \\ 0 \\ 1 \\ 4 \\ 0 \\ 0 \\ 0 \\ 4 \\ 0 \\ 0 \\ 0 \end{Bmatrix} \qquad (2.31)$$

According to Eq. (2.31), then the "master" (or "super") dof are dof #1 (which is followed by 2 "slave" dof), dof #4 (which is followed by 1 slave dof), dof #6 (which has no slave dof!), dof #7 (which is followed by 3 slave dof), and dof #11 (which is followed by 3 slave dof).

The skeleton FORTRAN code LDL^T (with full matrix) shown in Table 3A should be modified as shown in Table 3B for incorporating sparse and "Master" (or "Super") degree-of-freedom-strategies

Table 3B: Pseudo FORTRAN Skeleton Code
for Sparse LDL^T Factorization With Master dof Strategies

```
c ... Assuming row 1 has been factorized earlier
      DO 11 I = 2, N
         DO 22 K = Only those previous "master" rows which have contributions to
                   current row I
c ... Compute the multiplier(s) (Note: U represent $L^T$)
            NSLAVEDOF = MASTER(I) - 1
            XMULT = U (K,I) / U (K,K)
            $XMUL_m$ = U (K+m,I) / U(K+m, K+m)
c ... m = 1,2, ... NSLAVEDOF
            DO 33 J = appropriated column numbers of "master" row #K
               U (I,J) = U (I,J) - XMULT * U(K,J)
                                 - $XMUL_m$ * U (K+m,J)
   33       CONTINUE
            U (K,I) = $XMUL_m$
            U (K+m, I) = $XMUL_m$
   22    CONTINUE
   11 CONTINUE
```

2.11 NUMERICAL EVALUATIONS OF DIFFERENT GENERALIZED EIGEN-SOLVERS

Based upon the discussions in previous sections, practical finite element models (such as Exxon off-shore Structure [6], High Speed Civil Transport Aircraft [4], and a 2-D Reverberation Chamber [11] are used to evaluate the performance of the developed sparse eigen-solvers. Since the codes have been written in standard FORTRAN language (and without using any library subroutines), it can be ported to different computer platforms (such as SUN-Sparc-20, IBM-R6000/590, Intel Paragon, Cray-C90 etc...) with no (or minimum) changes to the codes.

The accuracy of the developed codes for solving generalized eigen equations can be measured by the Relative Error Norm (=R.E.N.) which can be computed as:

$$R.E.N. = \frac{\|K\phi - \lambda M\phi\|}{\|K\phi\|} \tag{32}$$

The basic subspace iteration code, given in Ref. [1], will be used as a based-line reference. This "basic" subspace iteration code [1] will be compared to the developed basic, "sparse" subspace iteration, and "sparse" Lanczos codes. It should be emphasized here that more advanced, faster version of Subspace Iteration software has also been reported in the literature [1]. Lumped masses are used in all examples in this section.

Example 1: Exxon Off-Shore Structure [6]

The finite element model for the Exxon structure has used extensively in earlier research works. The resulted system of generalized eigen-equations from the Exxon model has 23, 155 dof.

The number of nonzero terms of the original stiffness matrix is 809,427. Using the Nested-Dissection (ND) algorithm, the number of nonzero terms (including "fills'in" terms) is 10,826,014. The relative error norm (or R.E.N., defined in Eq. 32) and the wall-clock time are presented and explained in Figure 2. It should be noted here that on the IBM-R6000/590 workstation, vector processing capability is available, where as the vector processing capability is "not" available on the Sun Sparc-20 workstation.

Example 2: High Speed Civil Transport (HSCT) Aircraft [4]

The finite element model for the HSCT aircraft has been used extensively in earlier research works. The resulted system of generalized eigen equations from the HSCT model has 16,152 dof. The number of nonzero terms of the original stiffness matrix is 373,980. Using the Modified Minimum Degree (MMD) algorithm, the number of nonzero terms (including "fill-in" terms) is 2,746,286. The numerical performances of 3 generalized eigen-solvers are presented in Figures 3-4.

Figure 2: Exxon Model
(USTSU31, Sun-Sparc20 Workstation)

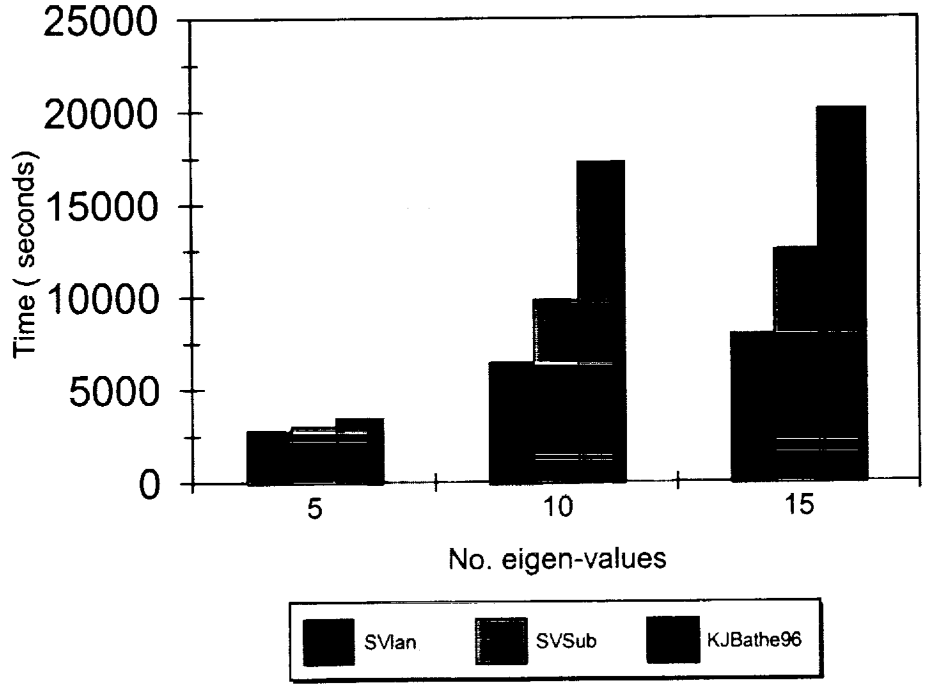

Figure 3: HSCT Aircraft model

(Stretch, IBM-R600/590 Worksation)

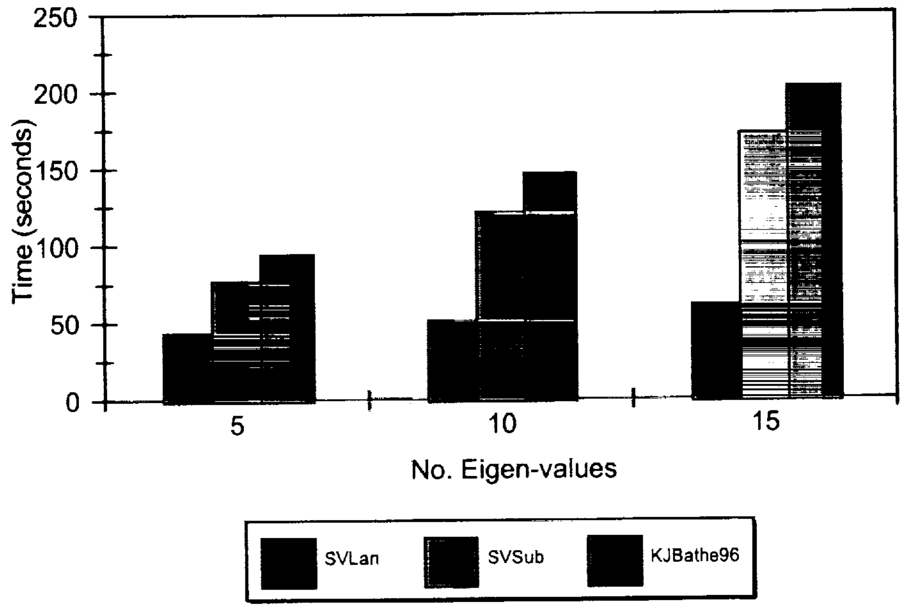

Figure 4: HSCT Aircraft model

(Rhino, ODU Sun Sparc-20 Worksation)

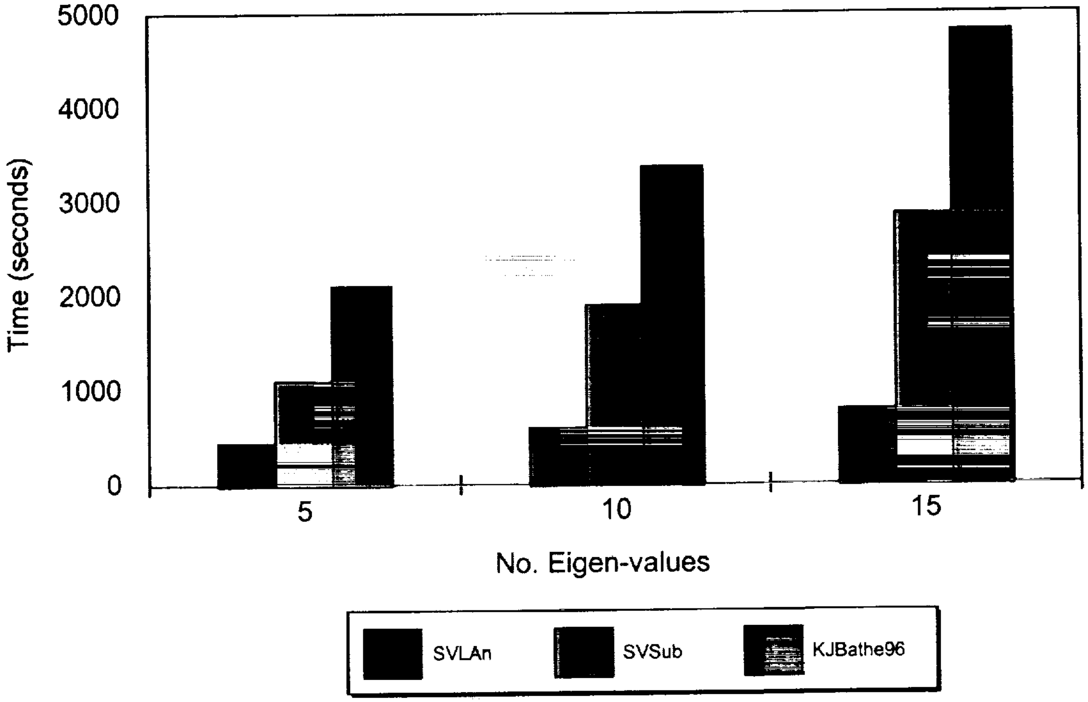

Example 3: A Two-Dimensional Reverberation Chamber (R.C.) [11]

The finite element model for the 2-D Reverberation Chamber (RC) has been used in earlier research works [11]. The resulted system of generalized eigen-equations from the R.C. model has 10,972 dof. The number of nonzero terms of the original "stiffness" matrix is 23,946. Using the MMD algorithm, the number of nonzero terms (including "fills-in" terms) is 165,135. The numerical performances of 3 generalized eigen-solvers are presented in Table 4.

Table 4: A 2-D R.C. Model

(Rhino, ODU Sun Sparc-20 Workstation, Consistent mass is used)

No. Eigen Values	Norfolk (Sun 3500/ODU), SV Lan (in seconds)	Rhino, ODU Sun Sparc-20 SV Sub (in seconds)	Rhino, ODU Sun Sparc-20 SV Lan (in seconds)
30	11.9sec	221	51
100	170.7	5,081	655
300	1502.8 (= 25min)	42,262	6,696

Example 4: A Simple Mathematical Data For Validating "Complex Numbers" Eigen-Solution Case

In this example one would like to solve the following generalized eigen value (12 degree-of-freedom) problem:

$$[K][\Phi] = [\lambda][M][\Phi]$$

where:

$$[K]\begin{bmatrix} (11.0,0.0)(0.,0.)\text{...........}(0.,0.) \\ (12.,0.)\text{......}(0.,0.) \\ (13.,0.) \\ (22.,0.) \end{bmatrix}_{12x12}$$

$$[M]\begin{bmatrix} (1.,0.)(0.,0.)\text{...........}(0.,0.) \\ (1.,0.)\text{.....}(0.,0.) \\ (1.,0.).(0.,0.) \\ sym \\ (1.,0.) \end{bmatrix}_{12x12}$$

The first 4 "complex" eigen values can be computed from the FORTRAN code as:

$$\lambda_1 = (11.0,0.0),\ \lambda_2 = (12.,0.),\ \lambda_3 = (13.,0.),\ \text{and } \lambda_4 = (14.,0.)$$

2.12 CONCLUSION

In this paper, basic generalized eigen-solution algorithms are reviewed. Major computational tasks in Subspace iterations, and Lanczos algorithms have been identified. Efficient sparse technologies have been developed, and fully utilized, in conjunction with the basic Subspace iterations and Lanczos algorithms (such as: sparse symbolic, numerical factorization with unrolling strategies, sparse forward & backward solutions, sparse matrix-vector multiplications etc...) for efficient solutions of the generalized eigen-equations. Numerical results from practical finite element models have clearly indicated that the proposed "sparse" Subspace iterations and Lanczos algorithms have offered substantial computational advantages over the traditional "skyline", or "variable bandwidth" strategies.

Both lumped and consistent mass formulation have been incorporated into our eigen-solution package. Furthermore, both stiffness and mass matrices can be provided with either real, or complex numbers.

Applying these advanced techniques will enable a thorough statistical analysis of the reverberation chamber fields. The estimated required order of the eigenvalve problem is very large (100,000) and is driven by the desire to model the large number of modes which exist at higher frequencies. The number of eigensolutions that can be accurately modeled is frequency limited.

Future work will include a complex eigensolver to model the typically lossy behavior of reverberation chambers and the resulting statistical field variations.

2.13 REFERENCES

[1] Bathe, J., Finite Element Procedures, Prentice-Hall, Englewood Cliffs, New Jersey (1996).

[2] Hughes, T.J.R., The Finite Element Method, Prentice-Hall, Englewood Cliffs, N.J. (1987).

[3] Nguyen, D.T. Qin, J., Chang, T.P.Y. and Tong, P., "Efficient Sparse Equation Solver With Unrolling Strategies For Computational Mechanics," ICES 97 International Conference, San Jose, Costa Rica (May 4-9, 1997).

[4] Storaasli, O.O., Nguyen, D.T., and Agarwal, T.K., "The Parallel Solution of Large-Scale Structural Analysis Problems on Supercomputers," AIAA Journal, Vol. 28, No.7, pp. 1211-1216 (July 1990).

[5] Tong, P., and Rossettos, J.N., Finite Element Method: Basic Technique and Implementation, the MIT Press, Cambridge, Massachusetts, and London, England.

[6] Wang, Chang, T.Y.P., and Tong,P., "Nonlinear Deformation Responses of Rubber Components by Finite Element Analysis," Computational Mechanics '95: Theory and Applications Proceedings of the International Conference on Computational Engineering Science. July 30-Aug. 3 '95, Hawaii, USA (Volume 2, pp.3135-3140).

[7] Reddy, C.J., Deshpaude, M.D., Cockrell, C.R., and Beck, F.B., “Finite Element Method For Eigen Value Problems In Electromagnetic,” NASA Technical Paper 3485, NASA Langley Research Center (Dec. 1994).

[8] Lehman, T.H., “A statistically theory of electromagnetic fields in complex cavities, “*EMP Interaction Notes*, No. 494, 1993.

[9] Duff, LS. and Stewart, G.W. (Editors), Sparse Matrix Proceedings 1979 SIAM (1979).

[10] George, J.A. and Liu, W.H., Computer Solution of Large Sparse Positive Definite Systems, Prentice-Hall, Englewood Cliffs, NJ. (1981).

[11] C.F. Bunting, K.J. Moeller, C.J. Reddy, and S.A. Scearce, “A two-dimensional finite element analysis of reverberation chambers,”IEEE Trans. Electromag. Compat., vol. 41, no. 4, pp. 280-289, Nov. 1999.

Chapter 3

Statistical Characterization And The Simulation Of A Reverberation Chamber Using Finite Element Techniques

3.1 INTRODUCTION

A reverberation chamber is an enclosure consisting of metal walls with a metallic paddle wheel (denoted a "stirrer" or "tuner") forming a high quality factor (Q) cavity with continuously variable boundary conditions. Reverberation chambers have attained increased importance in the determination of electromagnetic susceptibility of avionics equipment. This importance will become even more critical as advanced high-speed transport aircraft are developed that increasingly depend on electronic sensors and computer control of flight surfaces to manage the flight parameters.

The fields in a reverberation chamber are typically characterized by statistical means. Specifically the probability density functions for the real and imaginary components of a particular polarization of the electric and magnetic fields are normally distributed. The field magnitudes are Rayleigh distributed and the power is exponentially distributed. Reasonable statistical agreement for a source-free two-dimensional finite element model has been obtained and was the primary emphasis of the work presented by the author [1].

There are two focus areas that will be addressed in this work. The first problem to be briefly addressed in this paper is an examination of a two-dimensional finite element model for both the transverse electric (TE) and transverse magnetic (TM) solutions inside a reverberation chamber. A two-dimensional approach to the analysis of reverberation chambers was initially suggested by Wu [2] for mechanical stirring using the transmission line matrix (TLM) method. Hill [3] examined frequency stirring for an empty two-dimensional structure supporting TM modes. For the current work the fields (both TE and TM) in the cavity will be simulated with an emphasis on the tuner effects on the modal structure and the resulting statistics of the field distribution. The second focus is shielding effectiveness in a reverberating environment. Typical shielding effectiveness measurements are performed in a plane wave environment under various angles of incidence. The reverberating environment may provide additional insight into the shielding properties in a statistical sense.

The following section presents an overview of the computational tools used to simulate the reverberation environment. The TE results for the simulation "chamber" are then presented with an examination of coupling (fields inside vs. outside) shielding effectiveness through an aperture. The TM results are then presented for the simulation chamber. The application of a two-dimensional analysis tool may lead to useful investigations of stirrer efficiency, field homogeneity, and shielding effectiveness.

3.2 FINITE ELEMENT FUNDAMENTALS FOR TE AND TM FIELDS

The finite element method is a deterministic approach to the solution of Maxwell's equations using a weighted residual formulation over a set of compact-support basis functions to solve for the fields. Consider the geometry of Figure 3.3.1 with a source located at (x_0, y_0).

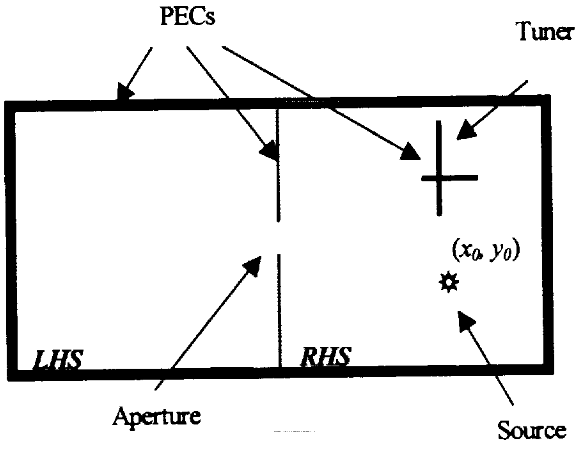

Figure 3.1. The 2D reverberation geometry

The electromagnetic field behavior is governed by Maxwell's equations as given by

$$\nabla \times \bar{E} = -j\omega\mu\bar{H}\,, \tag{3.1}$$

$$\nabla \times \bar{H} = j\omega\varepsilon\bar{E} + \bar{J}\,. \tag{3.2}$$

The inclusion of the source will be accomplished through the characteristics of the electric current density, $\bar{J}$, in eq. (3.2). By taking the curl of eq. (3.1) and substituting eq. (3.2) and assuming non-magnetic media the following inhomogeneous vector wave equation is obtained:

$$\nabla \times \left(\nabla \times \bar{E}\right) - k_0^2\varepsilon_r\bar{E} = -jk_0\eta_0\bar{J} \tag{3.3}$$

where $\bar{E}$ is the electric field intensity in volts/meter, k_0 is the wavenumber with $k_0 = \omega\sqrt{\mu\varepsilon}$, at a radian frequency ω, with permittivity ε and permeability μ, and intrinsic impedance η_0. The behavior of the electric field is of the form

$$\bar{E}(x,y,z) = \left[\bar{e}_t(x,y) + \hat{z}e_z(x,y)\right]e^{-\gamma z}.$$

Setting $\gamma = 0$ for cutoff and expressing the del operator as $\nabla = \nabla_t + \hat{z}\frac{\partial}{\partial z}$, it is possible to write two separate equations - one for the transverse part and another for the z component. The transverse field behavior is modeled with the use of edge elements and the z-directed fields are modeled using traditional node based elements. The expression of eq. (3.3) will depend on whether a TE or TM field will be considered to exist within the structure. This dependence completely rests in the expression of the electric current density, $\bar{J}$.

3.2.1 TE Fundamentals-a dipole source

The TE case can be expressed by considering a transverse electric current that can be thought of as a short dipole antenna with a uniform current density. In the TE case $\bar{J}$ can be expressed

$$\bar{J} = I_0\overline{J_T}$$

from which the eq. (3.3) is written

$$\nabla_t \times \left(\nabla_t \times \bar{e}_t\right) - k_0^2\varepsilon_r\bar{e}_t = -jk_0\eta_0 I_0\overline{J_T} \tag{3.4}$$

$$\nabla_t \bullet \left(\nabla_t e_z\right) + k_0^2\varepsilon_r e_z = 0\,. \tag{3.5}$$

Eq. (3.4) represents the transverse variation and the eq. (3.5) represents the z-directed variation. The transverse electric current exists only on the edge of a given element and is zero elsewhere.

Obtaining the weighted residual form involves integrating over the element support and assigning the continuity conditions. Integrating on an elemental basis is accomplished by

$$\iint\left[(\nabla_t \times \bar{e}_t)\bullet(\nabla_t \times \bar{T}_t) - k_0^2\varepsilon_r\bar{e}_t \bullet \bar{T}_t\right]ds = -jk_0\eta_0\iint\left[\bar{J}_T \bullet \bar{T}_t\right]ds \tag{3.6}$$

and

$$\iint\left[-(\nabla_t e_z)\bullet(\nabla_t T_z) + k_c^2\varepsilon_r e_z T_z\right]ds = 0 \tag{3.7}$$

Assigning continuity conditions and setting the fields to zero on the perfectly conducting walls and tuner yields a matrix equation of the form $\mathbf{A}\bar{\mathbf{x}} = \mathbf{b}$ for the transverse fields. Note that for this system that $\bar{\mathbf{x}} = \left\{E_x \quad E_y\right\}^T$ and that $E_z = 0$.

3.2.2 TM Fundamentals-an infinite line source

Following directly the work of Hill [3], the TM case uses an infinite line source located at (x_0, y_0) of the form

$$\bar{J} = \hat{z}I_0\delta(x - x_0)\delta(y - y_0). \tag{3.8}$$

so that (4) can be written as

$$\nabla_t \times (\nabla_t \times \bar{e}_t) - k_0^2\varepsilon_r\bar{e}_t = 0 \tag{3.9}$$

$$\nabla_t \bullet (\nabla_t e_z) + k_0^2\varepsilon_r e_z = -jk_0\eta_0 I_0\delta(x - x_0)\delta(y - y_0) \tag{3.10}$$

leading to the following weighted residual form:

$$\iint\left[(\nabla_t \times \bar{e}_t)\bullet(\nabla_t \times \bar{T}_t) - k_0^2\varepsilon_r\bar{e}_t \bullet \bar{T}_t\right]ds = 0 \tag{3.11}$$

and

$$\iint\left[-(\nabla_t e_z)\bullet(\nabla_t T_z) + k_c^2\varepsilon_r e_z T_z\right]ds = -jk_0\eta_0 I_0 T_z(x_0, y_0) \tag{3.12}$$

Note that in obtaining eq. (3.12), the integration required to obtain the right-hand side is trivial. The resulting linear system of equations is of the form $\mathbf{A}\bar{\mathbf{x}} = \mathbf{b}$. Note that for this system that $\bar{\mathbf{x}} = \left\{E_z\right\}^T$ and that $E_x = 0$ and $E_y = 0$.

3.3 TE DIPOLE SOURCE RESULTS

The application of the finite element technique to fields which are transverse electric (TE) will be presented in this section. The resulting fields, E_x and E_y, will be used in the two-dimensional TE finite element model of the reverberation chamber. Some measures of reverberation chamber performance include the statistical characterization of the fields, stirring ratio, field uniformity, the maximum to average ratio, and the normalized standard deviation [4]. Several of these measures will be applied to provide basic validation of the reverberating characteristics of the simulation "chamber". The shielding effectiveness in the simulation chamber will also be presented in the next sub-section. The 2D dipole source results are obtained by the rotation of the tuner for 225 steps in 1.6° increments, thus providing a full mechanical rotation of the tuner. The results represent the solution of the matrix equation corresponding to eq. (3.6) for each of the tuner positions at each frequency of interest. Consider the geometry of Figure 3.3.2 depicting the discretized structure to be analyzed with a typical result in Figure 3.3.3. Note that the results of Figure 3.3.3 are logarithmic and emphasize the field structure rather than the absolute field levels. The source is in the right-hand region at location (2, −1).

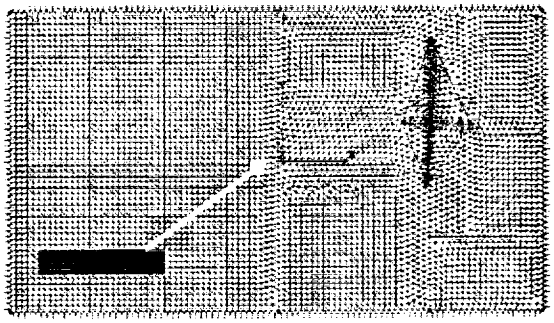

Figure 3.2. Discretized geometry of Figure 3.1.

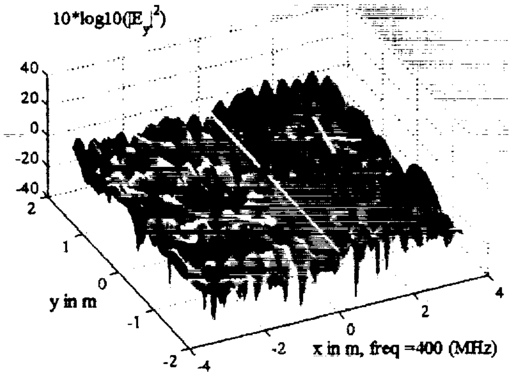

Figure 3.3. Fields for Figure 3.2 for a fixed tuner position.

3.3.1 Reverberation in the TE environment

There are several key factors governing reverberation characteristics and these factors can be used to determine if a chamber is operating properly. These factors include the stirring ratio, field uniformity, the ratio of the maximum field to average field, and the underlying statistical characterization of the fields. Of these measures of reverberation characteristics the stirring ratio and field uniformity will not be addressed in this paper. As the values of the field at particular point are plotted it was noted that strong numerical resonances occur throughout the computational domain in the lossless structure. These resonances correspond to the eigenvalues of the source-free problem [1]. In order to improve the numerical stability the quality factor, Q, can be altered by filling the chamber with lossy material ($\varepsilon = 1+j0.001$). The field statistics at a given point for 225 tuner steps is depicted in Figure 3.3.4.

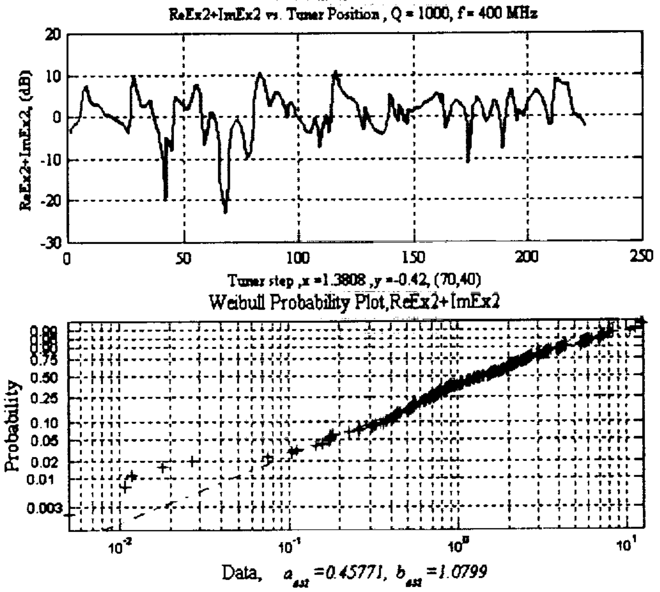

Figure 3.4. The statistical characteristics of the total TE field for a fixed point for 225 tuner positions.

The total squared electric field statistics at a point inside the shielded LHS are depicted with a Q of 1000 at a frequency of 400 MHz. The Weibull probability plot [1] shown at the bottom of Figure 3.3.4 is a strong indicator regarding the nature of a sample statistic. The probability plot helps eliminate ambiguities that may arise in interpreting agreement by comparing cumulative distribution functions (CDFs). The probability plot maps the parent distribution to a straight line and emphasizes differences in the tails of the sample distribution. Note that the + symbols on the plot represent the sample and all but approximately 2 % of the data are nearly collinear with the parent Weibull distribution. The Weibull density function is a more general density function that can fit a variety of bounded continuous distributions including the exponential distribution. The square of a particular component of the electric field, say E_x^2, can be written

$$E_x^2 = \mathrm{Re}\{E_x\}^2 + \mathrm{Im}\{E_x\}^2 . \tag{3.13}$$

If the underlying distributions for the real and the imaginary parts are N(0,1) then the squared sum is exponentially distributed as well as distributed as chi-squared with two degrees of freedom. The probability density function for an exponential distribution is

$$y = f(x|\mu) = \frac{1}{\mu} e^{-\frac{x}{\mu}} \tag{3.14}$$

with parameter μ.. The exponential distribution is a special case of a Weibull distribution given by the probability density function

$$y = \begin{cases} f(x|a,b) = abx^{b-1}e^{-ax^b} & ,x > 0 \\ 0 & ,x < 0 \end{cases} . \tag{3.15}$$

The exponential distribution corresponds to $b = 1$ in eq. (3.15). Considering the *x*-component of the electric field as depicted in Figure 3.3.4, the estimate of b_{est} =1.0799 is a good indicator of agreement with the expected distribution. It strongly suggests that the underlying distributions are indeed normally distributed. The CDF is plotted in Figure 3.3.5 showing a strong agreement with the expected Weibull distribution and the chi-squared distribution with two degrees of freedom. Another measure of reverberation quality is the normalized standard deviation σ_n is defined by

$$\sigma_n = \frac{\sigma}{\mu}$$

where σ is the sample standard deviation and μ is the sample mean. The point shown (70,40) in the right hand side (RHS), which is the complex portion of the structure, has a normalized standard deviation of 0.991. The ratio of the maximum to average field is 7.93 dB is shown in Figure 3.3.6 which agrees well the expected value of 8 dB. The stirrer ratio is 33.8907 dB which is indicative of excellent stirring within the complex RHS. A summary of example statistics for a few points in the structure is shown in Table 1. Table 1 portrays the Weibull parameters, the normalized standard deviation, the max-to-average ratio, and the stirring ratio for two points in each of the two major regions within the simulation chamber. The plots of Figures 4,5, and 6 represent the data for the point (70,40). Note the general excellent agreement for each of the points shown. Of particular interest is that the LHS is unstirred and it has generally identical statistical and reverberation characteristics as the complex RHS. This interesting result is suggestive of a form of "source" stirring wherein the fields appearing at the aperture joining the two regions acts with sufficiently random amplitude and structure as to excite a complex field in the non-complex region.

Table 3.1. Summary of statistical characteristics for the TE fields.

TE		Weibull Parameters					
Ref.	Coordinates	a	b	σ_n	MA(dB)	SR(dB)	
(20,40)	(-2.16, -0.42)	0.5033	0.9942	0.9724	7.302	35.35	} LHS
(40,40)	(-0.79, -0.42)	0.5429	0.9293	1.1933	9.505	32.43	
(70,40)	(1.38, -0.42)	0.4577	1.0799	0.9910	7.927	33.89	} RHS
(80,40)	(2.09, -0.42)	0.5280	0.9541	1.2551	9.255	29.00	

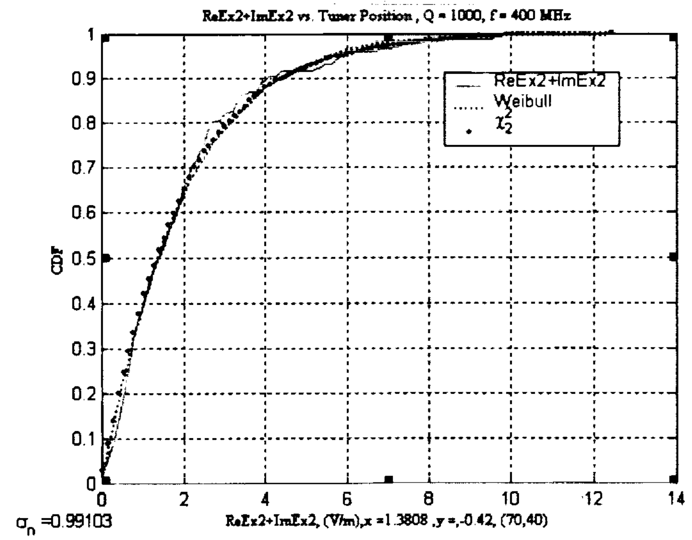

Figure 3.5. The cumulative distribution of the total TE field for a fixed point for 225 tuner positions.

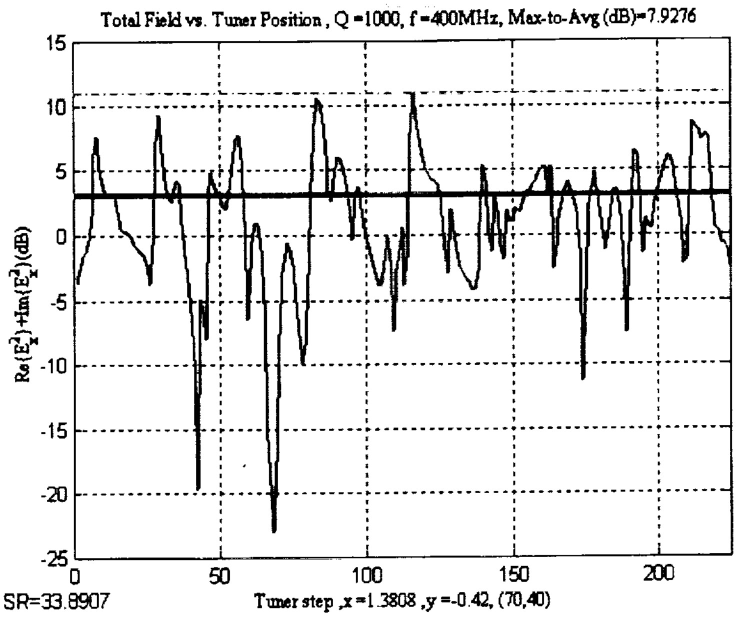

Figure 3.6. The total TE field for a fixed point for 225 tuner positions highlighting the max-to-average ratio and stirrer ratio.

Considering the field uniformity within each region can further highlight the idea of "source" stirring. In this study the field uniformity will be exploring by considering a test region in which the ensemble average of the fields is sampled and compared to other points within the test region. The fields will be considered to be uniform if the sample is with ± 3 dB of the average of all sample points. The test region is considered uniform if 75% of the sample field points are within the ± 3 dB region. The total electric field in the RHS is studied in Figure 3.3.7. The top of Figure 3.3.7 depicts the sample region wherein 100 points are chosen at random. Note that the wall with the aperture is not shown, but exists for reference points (50, Y). The uniformity is depicted in the bottom of Figure 3.3.7 with the circled data representing points within ± 3 dB of the average value of approximately –7 dB. The triangles indicate points that are outside the specified limits. As can be seen, 81 out of 100 points are within the limits and therefore the test region in the RHS can be considered to have a uniform field. The uniformity in the LHS is shown in Figure 3.3.8 with 91 % of the points falling within ± 3 dB of the average. The good result for the field uniformity in the non-complex LHS further suggests that "source" stirring can provide excellent reverberation characteristics.

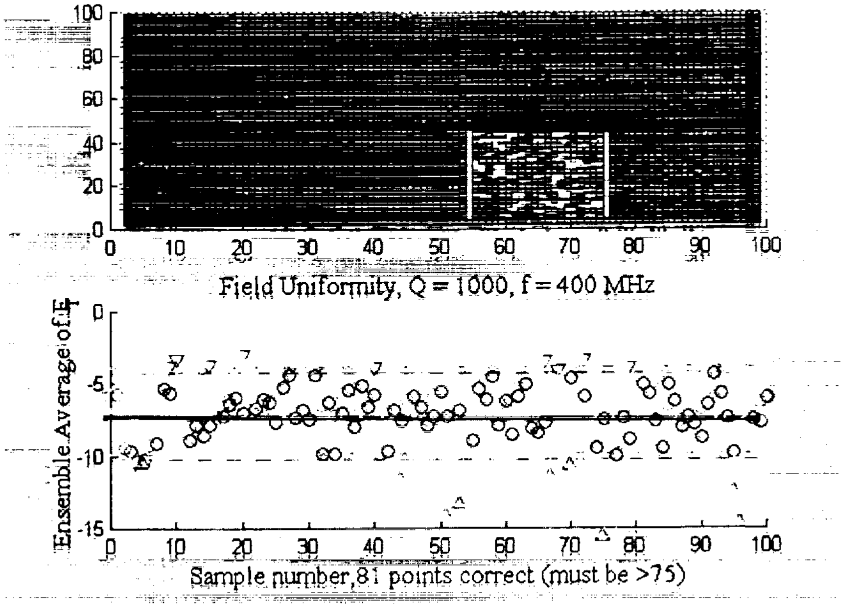

Figure 3.7. ±3 dB Field uniformity of the total TE field for 100 points in the RHS for 225 tuner positions.

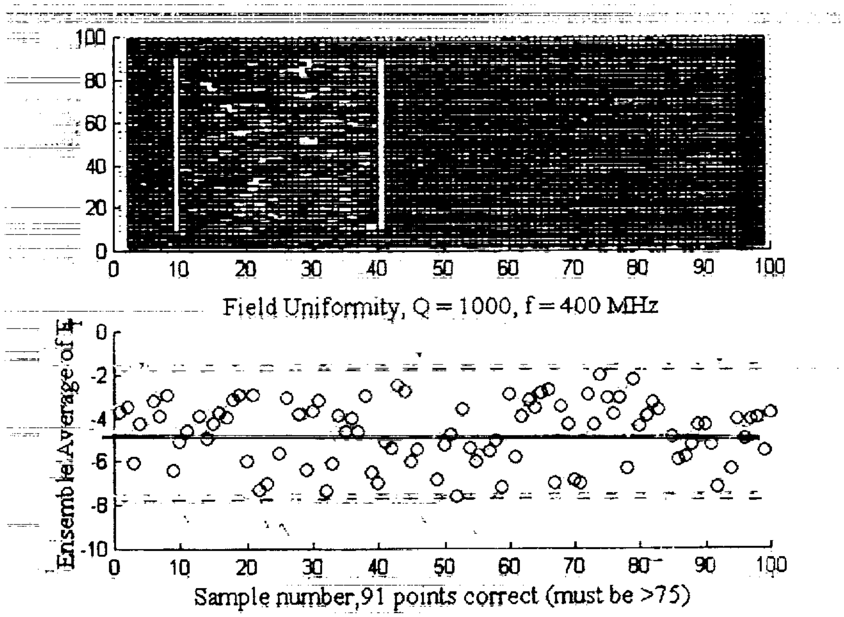

Figure 3.8. ±3 dB Field uniformity of the total TE field for 100 points in the LHS for 225 tuner positions.

3.3.2 Shielding Effectiveness for the TE structure

The application to the problem of coupling shielding effectiveness via an aperture will be examined in this section. The geometry of Figure 3.1 is the geometry under consideration for this examination. Consider a set of random points in the source region (RHS). For those fixed points there will be some maximum field level that will exist over all tuner positions. This level represents the maximum level in the source region. Consider taking another set of random points in the test region (LHS). This set consists of the individual maximums for each test point for all tuner positions. A typical result for the shielding effectiveness of the maximums can be seen in Figure 3.9. Interestingly there are 22 occurrences of negative shielding effectiveness out of the total of 100 random points chosen. This is indicative of phenomena wherein the field is larger in the shielded test region than in the source region. The average shielding effectiveness of the maximums was 2.19dB for 400 MHz.

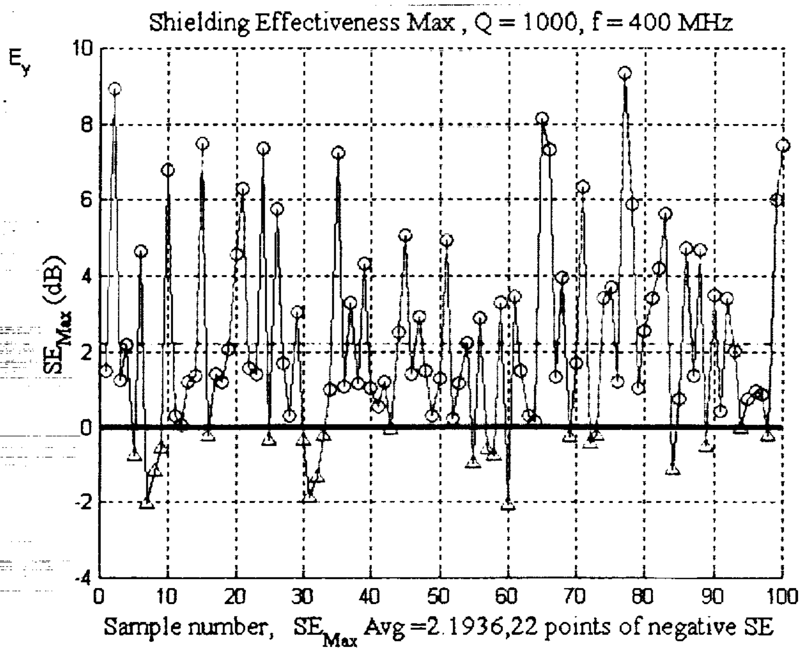

Figure 3.9. Shielding effectiveness of the maximums for the TE field.

3.4 TM INFINITE LINE-SOURCE RESULTS

The work presented in this section will examine the statistics of the TM fields in the two-dimensional reverberation structure. This work closely follows the work of Hill in that the only surviving field component is E_z. The results presented in this section will exactly parallel the work on the TE fields previously shown, so developmental discussions will be omitted.

3.4.1 Reverberation in the TM environment

The field solution for the TM problem consists of the z-component of the electric field with real and imaginary parts. The field statistics for the TM case are shown in Figure 3.10 for reference point (70,30). The estimate of the shape parameter b_{est} = 0.50945 for the Weibull distribution indicates that one or more of the underlying distributions is not normally distributed. This result is consistent with Hill's results when the frequency chosen is such that an insufficient number of modes exist within the structure. It is significant to note that the field levels for the TM problem are several orders of magnitude larger than the TE problem. The CDF of the sample is depicted in Figure 3.11 in comparison with the Weibull distribution and the chi-squared distribution with the normalized standard deviation of 2.3413. The maximum to average ratio is shown in Figure 3.12 and is 12.34 dB. The stirrer ratio is also portrayed in Figure 3.12 and has a value of 49.56 dB. Table 2 depicts several points in various points within the geometry similar to those shown earlier with similar results for the fields in the complex RHS and the non-complex LHS.

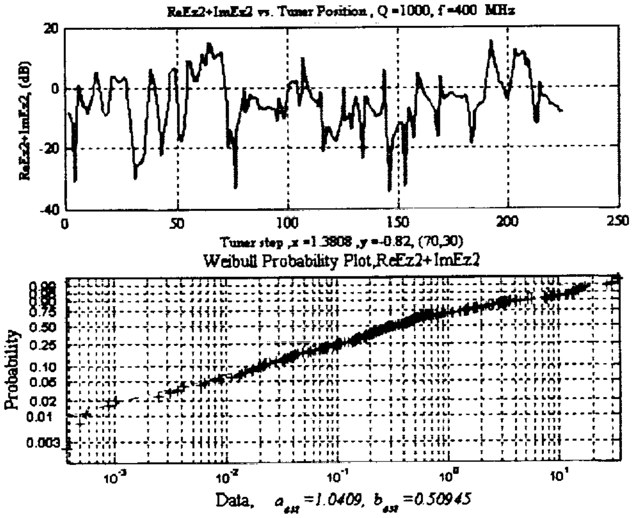

Figure 3.10. The statistical characteristics of the total TM field for a fixed point for 225 tuner positions.

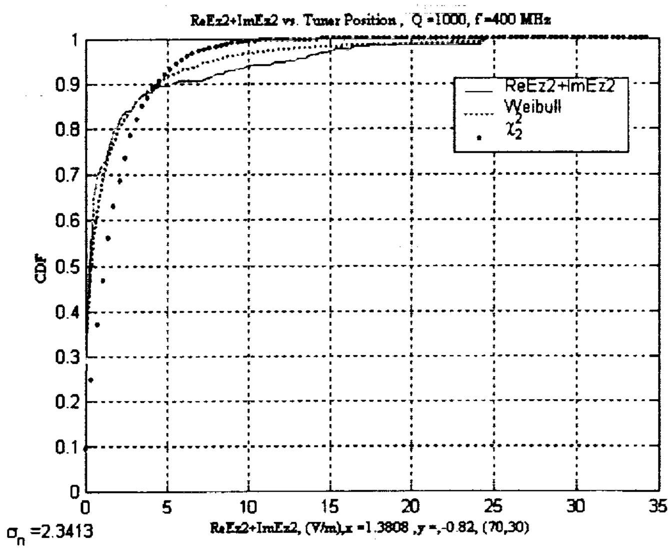

Figure 3.11. The cumulative distribution of the total TM field for a fixed point for 225 tuner positions.

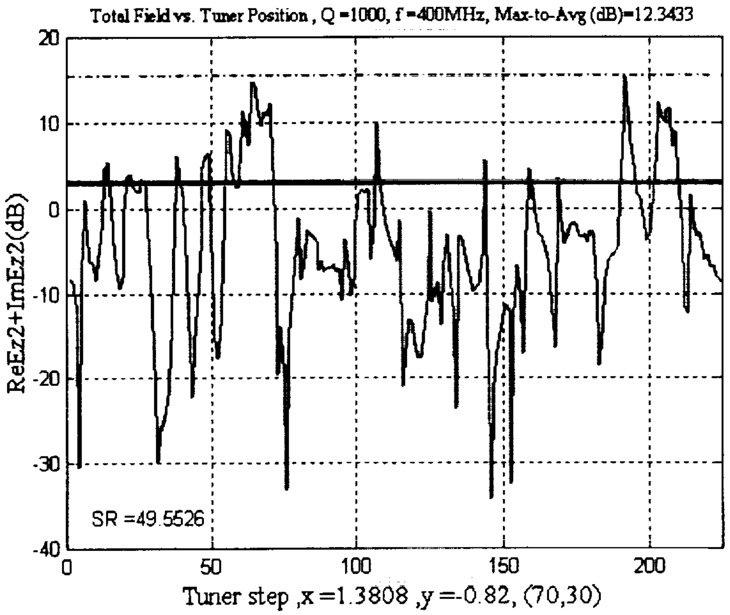

Figure 3.12. The total field total TM field for a fixed point for 225 tuner positions highlighting the max-to-average ratio and stirrer ratio.

Table 3.2. Summary of statistical characteristics for the TM fields.

TM		Weibull Parameters					
Ref.	Coordinates	a	b	σ_n	MA(dB)	SR(dB)	
(20,40)	(-2.16, -0.42)	1.042	0.509	2.3479	12.38	48.68	} LHS
(40,40)	(-0.79, -0.42)	1.043	0.508	2.3461	12.36	50.36	
(70,30)	(1.38, -0.82)	1.041	0.509	2.3413	12.34	49.55	} RHS
(80,40)	(2.09, -0.42)	1.043	0.508	2.3454	12.36	50.51	

The field uniformity in the RHS and LHS are studied in Figures 13 and 14. Note that the RHS has 63 % uniformity in Figure 3.13 and the LHS has 59 % uniformity. These results combine to raise some basic questions regarding the statistical characteristics of the TM model at the frequencies used, and are the subject of a more detailed exploration in the following paragraph.

Further examination revealed that the real and imaginary parts of E_z is distributed according to a Johnson SU distribution [5,6]. The Johnson distribution is denoted S_U and is a four parameter distribution with a probability density function

$$f(x)=\frac{\alpha_2}{\sqrt{2\pi}\sqrt{(x-\gamma)^2+\beta^2}}\exp\left\{-\frac{1}{2}\left[\alpha_1+\alpha_2\ln\left(\frac{x-\gamma}{\beta}+\sqrt{\left(\frac{x-\gamma}{\beta}\right)^2+1}\right)^2\right]\right\} \tag{3.16}$$

for all real numbers x. The parameters are a location parameter $\gamma\in(-\infty,\infty)$, scale parameter $\beta>0$, and shape parameters $\alpha_1\in(-\infty,\infty)$, and $\alpha_2>0$. The CDF is given by

$$F(x)=\Phi\left\{\alpha_1+\alpha_2\ln\left(\frac{x-\gamma}{\beta}+\sqrt{\left(\frac{x-\gamma}{\beta}\right)^2+1}\right)\right\}, \tag{3.17}$$

with $\Phi(z)$ the standard normal distribution function. The skewness of the density function is represented in the shape parameter α_1 with the density function skewed left when $\alpha_1>0$, symmetrical when $\alpha_1=0$, and skewed right when $\alpha_1<0$. Tables 3 and 4 depict the summary statistics for the real and imaginary parts, respectively. These results depict a wide variation of the parameters for various locations within the structure. Work is ongoing to ascertain the connection that can possibly be made between these results and an undermoded reverberation chamber.

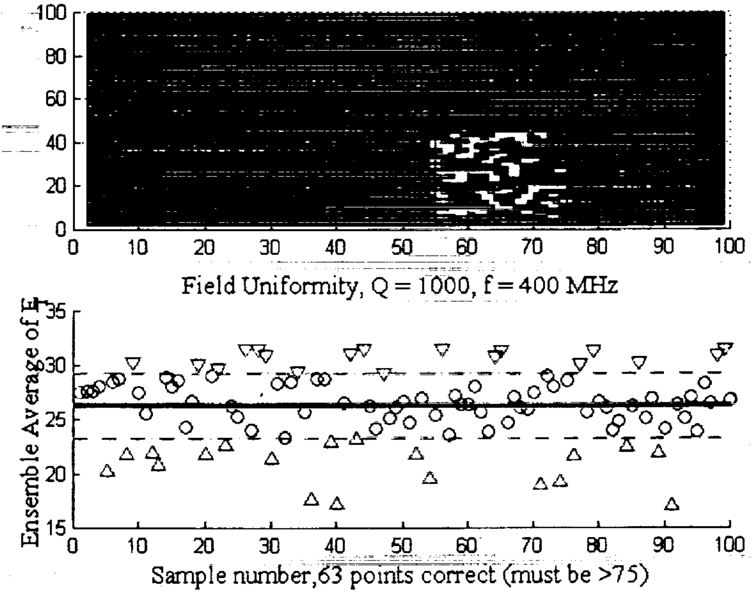

Figure 3.13. ±3 dB Field uniformity of the total TM field for 100 points in the RHS for 225 tuner positions.

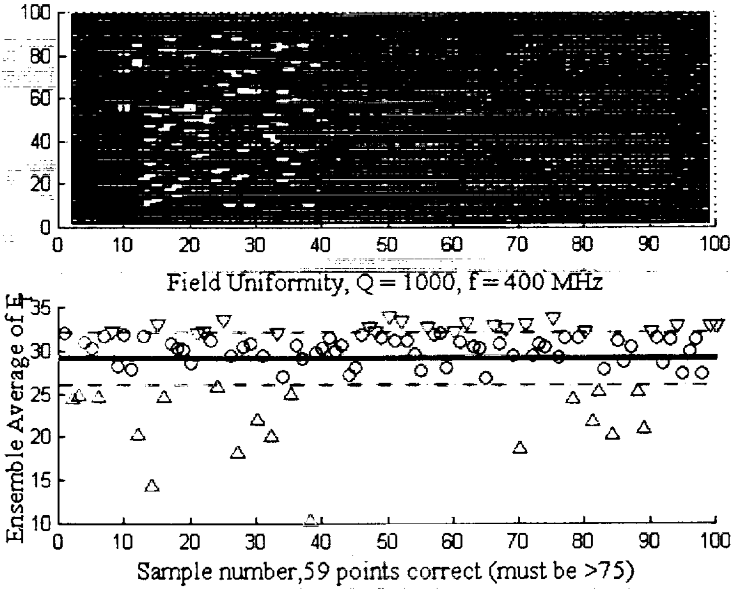

Figure 3.14. ±3 dB Field uniformity of the total TM field for 100 points in the LHS for 225 tuner positions.

Table 3.3. Summary of statistical characteristics for the real part of the TM fields.

Re$\{E_Z\}$		Johnson S_U Parameters				
Ref.	Coordinates	γ	β	α_1	α_2	
(20,40)	(-2.16, -0.42)	14.98	17.93	-0.5110	0.4818	} LHS
(40,40)	(-0.79, -0.42)	-52.77	63.63	0.5249	0.4903	
(70,30)	(1.38, -0.82)	11.93	26.33	-0.6526	0.5331	} RHS
(80,40)	(2.09, -0.42)	-34.69	43.59	0.5366	0.4931	

Table 3.4. Summary of statistical characteristics for the imaginary part of the TM fields.

Im$\{E_Z\}$		Johnson S_U Parameters				
Ref.	Coordinates	γ	β	α_1	α_2	
(20,40)	(-2.16, -0.42)	-148.64	199.28	-0.2355	0.9527	} LHS
(40,40)	(-0.79, -0.42)	506.07	651.37	0.2439	0.9361	
(70,30)	(1.38, -0.82)	-186.49	203.49	-0.2830	0.8880	} RHS
(80,40)	(2.09, -0.42)	345.93	441.17	0.2482	0.9342	

3.4.2 Shielding Effectiveness for the TM structure

The shielding effectiveness of the maximums for the TM field is depicted in Figure 3.15. The resulting coupling appears to be much stronger for and identical test configuration. The average shielding effectiveness is seen to be 0.991 dB with 40 points out of 100 demonstrating negative shielding effectiveness.

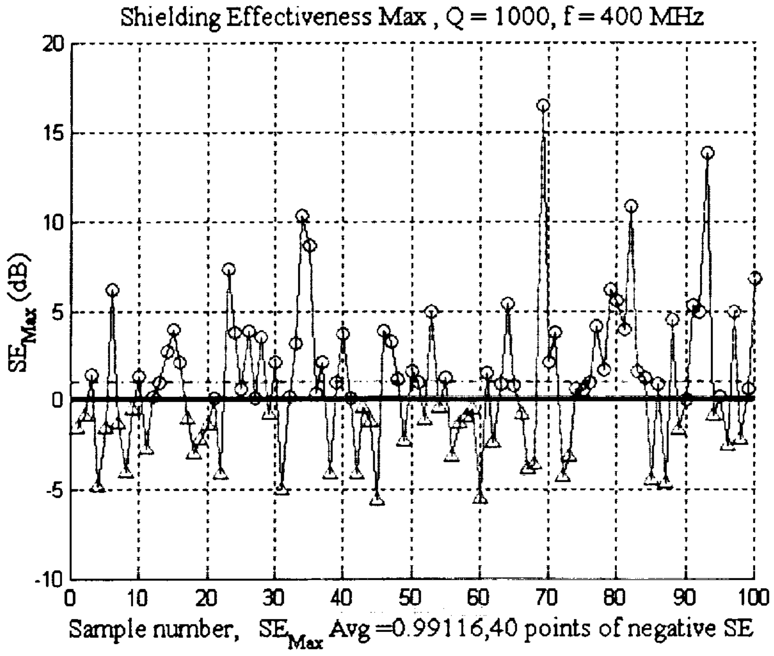

Figure 3.15. Shielding effectiveness of the maximums for the TM field.

3.5 CONCLUSIONS

A two-dimensional finite element model for both the transverse electric (TE) and transverse magnetic (TM) solutions inside a simulation reverberation chamber has been presented. Tuner effects on the modal structure and the resulting statistics of the field distribution have been explored. It was demonstrated that the TE simulation reverberation chamber provided excellent statistical and reverberation characteristics. The measures of reverberation characteristics included normalized standard deviation, the max-to-average ratio, the stirrer ratio, and the field uniformity. In addition the notion of “source” stirring was introduced wherein the fields that were coupled into the non-complex geometry were shown to be statistically similar to those in the complex environment. The idea of source stirring may shed light on the question of whether it is absolutely necessary to stir in all regions that a reverberation type test is being performed. The practical issues are enormous when considering the demands that internal stirring may place on the testing regimen. The TM simulation chamber did not satisfy any of the required reverberation characteristics, and the field components were shown to be distributed according to a Johnson S_U distribution. Further study may link the results of the TM simulation chamber to an undermoded reverberation chamber and may be useful in extending the useful low frequency of the reverberation chamber. The shielding effectiveness in a reverberating environment was been examined. Coupling shielding effectiveness for TE and TM results was presented. The reverberating environment provides additional insight into the shielding properties in a statistical sense.

3.6 REFERENCES

[1] Bunting, C.F., K.J. Moeller, C.J. Reddy, and S.A. Scearce, "A two-dimensional finite element analysis of reverberation chambers", *IEEE Trans. Electromag. Compat.*, vol. 41, pp. 280-289.

[2] D.L. Wu and D.C. Chang, "The effect of an electrically large stirrer in a mode-stirred chamber," *IEEE Trans. on Electromag. Compat.*, vol. 31, no. 2, pp. 164-170, 1989.

[3] D.A. Hill, "Electronic mode stirring for reverberation chambers," *IEEE Trans. on Electromag. Compat.*, vol. 36, pp. 294-299, 1994.

[4] M. O. Hatfield, G.J. Freyer, and M.B. Slocum, "Reverberation characteristics of large welded steel shielded enclosures," *Proc. of the IEEE 1997 Intl. Symposium on Electromag. Compat.* pp. 38 – 43, Austin TX, 1997.

[5] Averill M. Law and W. David Kelton, *Simulation Modeling and Analysis* (Third Edition) by McGraw-Hill (2000).

[6] Johnson, N.L., S. Kotz, and N. Balakrishnan, *Continuous Univariate Distributions*, Volume 2, Second Edition, Houghton Mifflin, Boston (1995).

Chapter 4

Shielding Effectiveness In A Reverberation Chamber Using Finite Element Techniques

4.1 INTRODUCTION

A reverberation chamber is an enclosure consisting of metal walls with a metallic paddle wheel (denoted a "stirrer" or "tuner") forming a high quality factor (Q) cavity with continuously variable boundary conditions. Reverberation chambers have attained increased importance in the determination of electromagnetic susceptibility of avionics equipment. This importance will become even more critical as advanced high-speed transport aircraft are developed that increasingly depend on electronic sensors and computer control of flight surfaces to manage the flight parameters.

Shielding of avionics equipment from both interior and exterior electromagnetic threats is an important part of the system reliability budget. It is typically assumed that the shielding effectiveness of a structure has a level that is a function of frequency for various angles of incidence. Measurements in an anechoic chamber and analysis using computational methods simulate a plane wave environment to quantify shielding effectiveness. An investigation has been performed [1] suggesting that an under certain conditions the aircraft fuselage behaves as a reverberation chamber when stirred internally. Another investigation [2] revealed that the fields in an aircraft flown in the vicinity of a transmitting antenna have levels with characteristics that are statistically similar to a reverberation environment. A conclusion that may be drawn from this is that an aircraft fuselage is a structure in which the interior fields are not plane waves. This significant connection raises an interesting question: What is the shielding effectiveness of an aperture in a reverberating environment? The emphasis of this paper is the examination of a two-dimensional finite element model of a reverberation chamber to explore the shielding effectiveness of an aperture over a variety of frequencies in a TM field configuration.

The fields in a reverberation chamber are typically characterized by statistical means. Specifically the probability density functions for the real and imaginary components of a particular polarization of the electric and magnetic fields are normally distributed. The field magnitudes are Rayleigh distributed and the power is exponentially distributed. Reasonable statistical agreement for a two-dimensional finite element model has been obtained and was the primary emphasis of the work presented by the author [3] for a source free problem. The field statistics for the TM model will not be developed in this work.

A two-dimensional approach to the analysis of reverberation chambers was initially suggested by Wu [4] for mechanical stirring using the transmission line matrix (TLM) method. Hill [5] examined frequency stirring for an empty two-dimensional structure supporting TM modes by defining the 2D Green's function for the rectangular structure. For the current work the fields in the cavity will be simulated as transverse magnetic (TM) with an emphasis on the tuner effects on the modal structure and the resulting shielding effectiveness in a reverberating environment. Typical shielding effectiveness measurements are performed in a plane wave environment under various angles of incidence. The reverberating environment may provide additional insight into the shielding properties in a statistical sense. Park [6] recently published results for the simulation of the shielding effectiveness of a two-dimensional TM structure in a plane wave environment. Interestingly he compared the simulated two-dimensional results with measured results. Based on Park's work, the shielding effectiveness of the TM structure via aperture coupling for several frequencies in a simulated reverberation environment will be examined. Measurements were also performed in NASA's reverberation chamber and are presented to provide a connection to the simulated statistical results.

The following section presents an overview of the computational tool used to simulate the reverberation environment. The TM results are then presented for the simulation chamber and the replacement (fields in box vs. fields with no box) shielding effectiveness is explored. A comparison of the TM results to an anechoic environment is made. Finally a comparison to measured results in NASA's reverberation chamber are presented. These results will point to the development of a statistical model of shielding effectiveness that will form a critical component to the overall mechanism of upset prediction in digital systems.

4.2 FINITE ELEMENT FUNDAMENTALS FOR TM FIELDS

The finite element method is a deterministic approach to the solution of Maxwell's equations using a weighted residual formulation over a set of compact-support basis functions to solve for the fields. Consider the geometry of Figure 4.1 with a source located at (x_0, y_0).

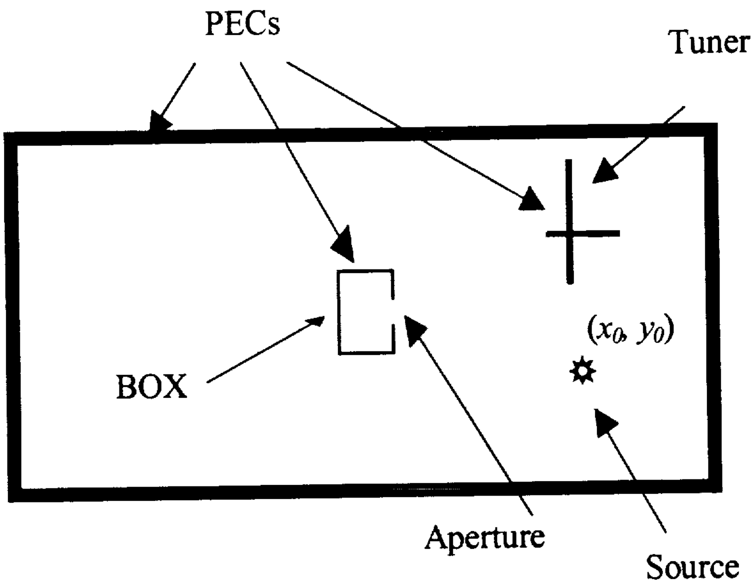

Figure 4.1. Geometry for the TM problem.

The electromagnetic field behavior is governed by Maxwell's equations as given by

$$\nabla \times \bar{E} = -j\omega\mu\bar{H}\,, \tag{4.1}$$

$$\nabla \times \bar{H} = j\omega\varepsilon\bar{E} + \bar{J}\,. \tag{4.2}$$

The inclusion of the source will be accomplished through the characteristics of the electric current density, $\bar{J}$, in eq. (4.2). By taking the curl of eq. (4.2) and substituting eq. (4.1) and assuming non-magnetic media the following inhomogeneous vector wave equation is obtained:

$$\nabla \times \left(\nabla \times \bar{E}\right) - k_0^2\varepsilon_r\bar{E} = -jk_0\eta_0\bar{J} \tag{4.3}$$

where $\bar{E}$ is the electric field intensity in volts/meter, k_0 is the wavenumber with $k_0 = \omega\sqrt{\mu\varepsilon}$, at a radian frequency ω, with permittivity ε and permeability μ, and intrinsic impedance η_0. The behavior of the electric field is of the form

$$\bar{E}(x,y,z)=\left[\bar{e}_t(x,y)+\hat{z}e_z(x,y)\right]e^{-\gamma z}.$$

Setting $\gamma = 0$ for cutoff and expressing the del operator as $\nabla=\nabla_t+\hat{z}\frac{\partial}{\partial z}$, it is possible to write two separate equations - one for the transverse part and another for the z component. The transverse field behavior is modeled with the use of edge elements and the z-directed fields are modeled using traditional node based elements. The particular form of the expression of eq. (4.3) will depend on whether a TE or TM field will be considered to exist within the structure. This dependence completely rests in the expression of the electric current density, $\bar{J}$.

4.2.1 TM Fundamentals-an infinite line source

Following the work of Hill [5], the TM case uses an infinite line source located at (x_0,y_0) of the form

$$\bar{J}=\hat{z}I_0\delta(x-x_0)\delta(y-y_0). \tag{4.4}$$

so that (4) can be written as

$$\nabla_t\times(\nabla_t\times\bar{e}_t)-k_0^2\varepsilon_r\bar{e}_t=0 \tag{4.5}$$

$$\nabla_t\bullet(\nabla_t e_z)+k_0^2\varepsilon_r e_z=-jk_0\eta_0 I_0\delta(x-x_0)\delta(y-y_0) \tag{4.6}$$

leading to the following weighted residual form:

$$\iint\left[(\nabla_t\times\bar{e}_t)\bullet(\nabla_t\times\bar{T}_t)-k_0^2\varepsilon_r\bar{e}_t\bullet\bar{T}_t\right]ds=0 \tag{4.7}$$

and

$$\iint\left[-(\nabla_t e_z)\bullet(\nabla_t T_z)+k_c^2\varepsilon_r e_z T_z\right]ds=-jk_0\eta_0 I_0 T_z(x_0,y_0) \tag{4.8}$$

Note that in obtaining eq. (4.8), the integration required to obtain the right-hand side is trivial. The resulting linear system of equations is of the form $\mathbf{A\bar{x}}=\mathbf{b}$. Note that for this system that $\mathbf{\bar{x}}=\{E_z\}^T$ and that $E_x = 0$ and $E_y = 0$.

4.3 TM INFINITE LINE-SOURCE RESULTS

This section presents a TM analysis that will compute the shielding effectiveness of a box with a single aperture. The 2D infinite line-source results are obtained by the rotation of the tuner for 225 steps in 1.6° increments, thus providing a full mechanical rotation of the tuner. The results represent the solution of the matrix equation corresponding to eq. (4.8) for each of the tuner positions at each frequency of interest. Consider the geometry of Figure 4.2 depicting the discretized structure to be analyzed with a typical result in Figure 4.3 for a frequency of 400 MHz. Note that the results of Figure 4.3 are logarithmic and emphasize the field structure rather than the absolute field levels. The close-up of the Box in Figure 4.4 demonstrates the field structure in the "shielded" box. Note that at 400 MHz the 10 cm aperture is 0.133 wavelengths long. Figures 4.5 and 4.6 depict similar results for a frequency of 600 MHz. Note that the field structure for 600 MHz is significantly more complex and that the mode structure inside the box demonstrates the existence of the TM_{11} mode. This indicates that there is one resonance inside the box between 400 MHz and 600 MHz, which actually occurs at 480.21 MHz.

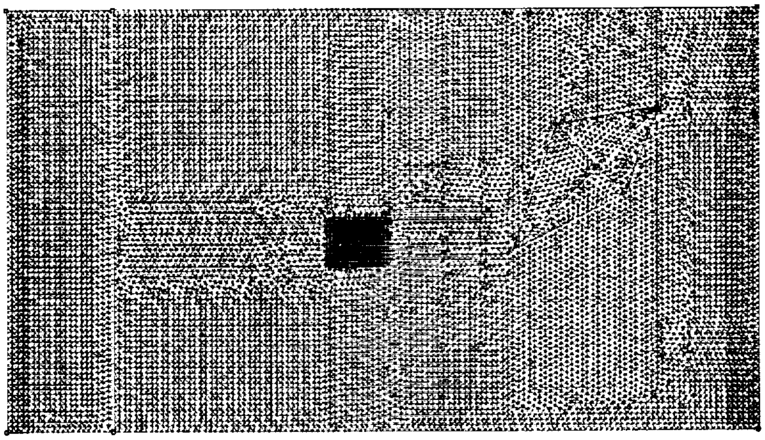

Figure 4.2. Discretized geometry for Figure 4.1. Grid is such that there are 10 samples per wavelength.

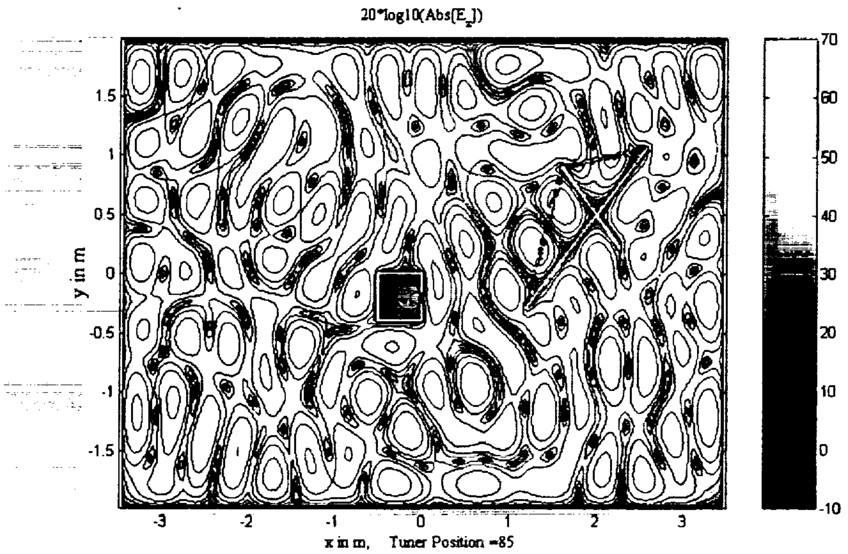

Figure 4.3. TM excitation at 400 MHz of a PEC box with an aperture.

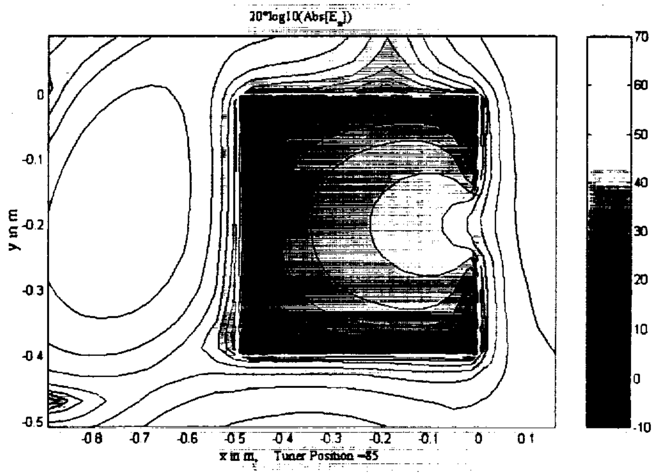

Figure 4.4. Close-up of PEC box with aperture at 400 MHz.

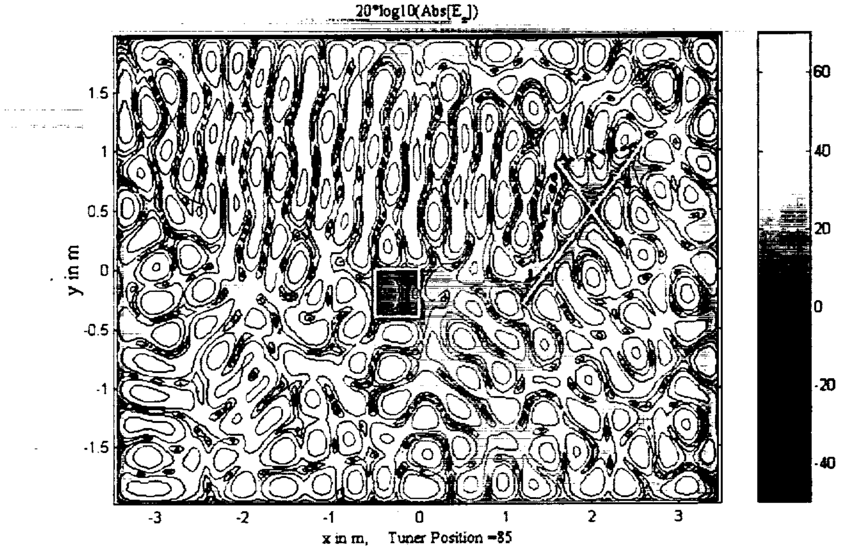

Figure 4.5. TM excitation at 600 MHz of a PEC box with an aperture.

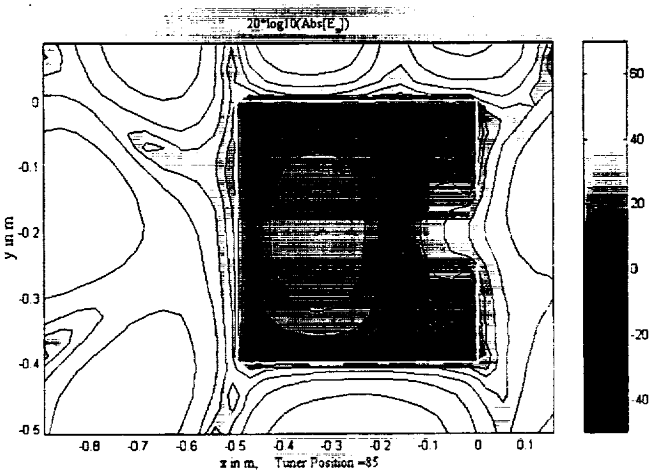

Figure 4.6. Close-up of PEC box with aperture at 600 MHz.

4.4 SHIELDING EFFECTIVENESS FOR THE TM STRUCTURE

This section will explore replacement-shielding effectiveness where the fields are simulated with and without the box present. This work follows closely the work of Park [6] who performed a plane wave analysis of a two-dimensional TM box with single and multiple apertures. Park also performed measurements that verified his computational results. This section will duplicate Park's test configuration, but with the significant difference of applying a reverberation chamber simulation. Measurements in NASA's medium size reverberation chamber (Chamber B) are presented to further corroborate the simulation. The shielding effectiveness (SE) simulation will explore the SE of a two-dimensional box that is 40 cm × 50 cm with a 10 cm aperture as depicted in Figure 4.1.

Simulations were performed at various frequencies with the shielding effectiveness defined as

$$SE = 20 * \log\left(\frac{E_Z^{NoBox}}{E_Z^{Box}}\right), \tag{4.9}$$

with the *NoBox* solution corresponding to the solution obtained with no box present and the *Box* solution for the fields at the center of the box. Typical results are portrayed in Figures 4.7 and 4.8. Figure 4.7 shows a comparison of the *z*-component of the electric field for the shielded and unshielded measurement. Note that these simulated results indicate roughly a 30 dB difference between the *Box* and *NoBox* cases. The results provide some interesting insight as to the nature of SE in a reverberation chamber. Note from Fig. 8 that the SE is normally distributed as seen from the linearity of the sample data on the normal probability plot and the subsequent histogram. The mean value of the SE is 35.3 dB with a standard deviation of 10.51 dB. Park's result is approximately 43 dB and is 7.7 dB greater than the more conservative mean obtained by the simulation. The 7.7 dB difference is well within a standard deviation from the simulated data. From Fig. 8 it can also be seen that the SE is less than 10 dB for tuner positions 25 and 71, and is nearly zero for position 71. The variation in SE is not attributable to resonance conditions since the first mode of the box is at 480.23 MHz. The fields in the aperture are varying continuously in amplitude and structure as the tuner is stirring the fields. Although the simulated frequency is below the cutoff of single mode operation in the box a statistical distribution of the field is obtained inside due to what may be considered "source" stirring. This form of stirring is distinct from frequency stirring [4] since the frequency in the simulation is fixed. The fields in the aperture have a statistical distribution governed by the characteristics of the simulation reverberation chamber and provide an excitation to the smaller non-complex cavity. This excitation drives the non-complex box in a manner consistent with large, complex reverberation chambers. An important conclusion to the idea of source stirring is that internal stirring of the non-complex box is not required.

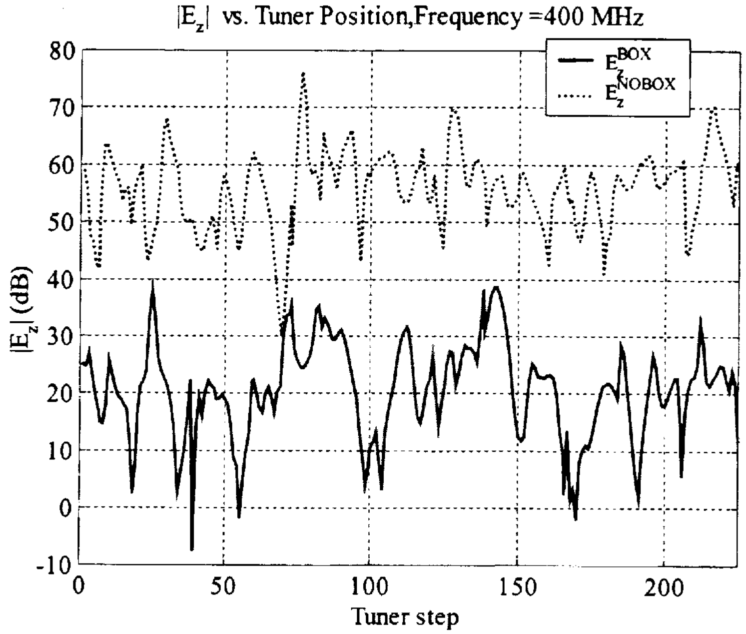

Figure 4.7. Magnitude of E_z for the shielded and unshielded cases at 400 MHz at the center of the box.

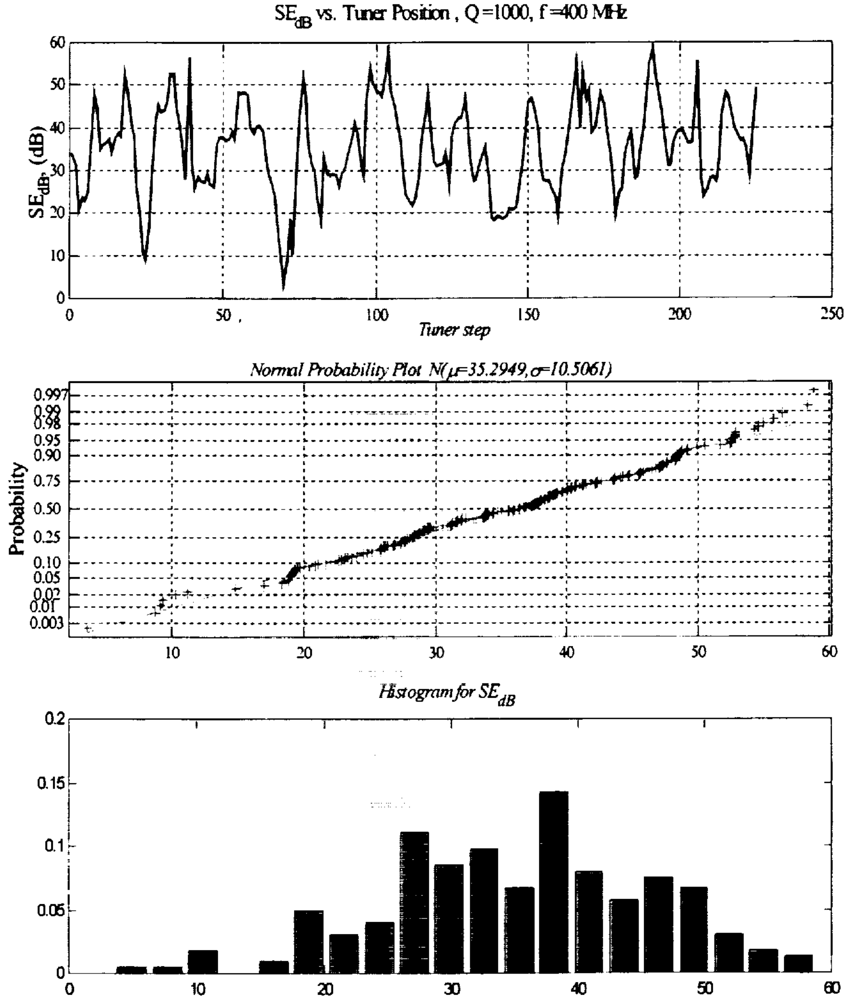

Figure 4.8. Shielding effectiveness for the Park [4] box at 400 MHz.

4.4.1 Measurements

This section will highlight the measurement of shielding effectiveness in the reverberation chamber. These measurements were performed on a rectangular box (40 cm × 50 cm × 20 cm) with an aperture that is 10 cm × 2 cm as depicted in Figure 4.9.

Figure 4.9. Box with aperture for shielding effectiveness measurements in the reverberation chamber.

For this measurement an HP 8720C vector network analyzer (VNA) was used to measure the transmission characteristics (S_{21}) in the chamber. The VNA was calibrated using "Response and Isolation". The measurement consists of a log-periodic antenna (transmit) to a probe (receive) located in the box at three positions: top, side, and rear wall for shielded measurements and then a measurement without the box for an unshielded measurement. The SE can be computed by a slight variation of eq. (4.9).

$$SE = 20 * \log\left(\frac{S_{21}^{NoBox}}{S_{21}^{Box}}\right) \tag{4.10}$$

for each wall position. A typical result at 400 MHz is depicted in Figure 4.10. A comparison of the SE reported by Park [6] and the simulated and measured results are presented in Figure 4.11. The Park data overestimates the SE for all but 500 MHz and is 28 dB higher than the simulated finite element model at 100 MHz. The simulated and measured results are nearly identical at 300 and 400 MHz, but diverge at the low and higher frequencies. The simulated results are 17 dB higher than the measured results at 100 MHz, and are 5 dB lower at 600 MHz. Further analysis would readily discern the resonance observed in the measured data at 450 MHz.

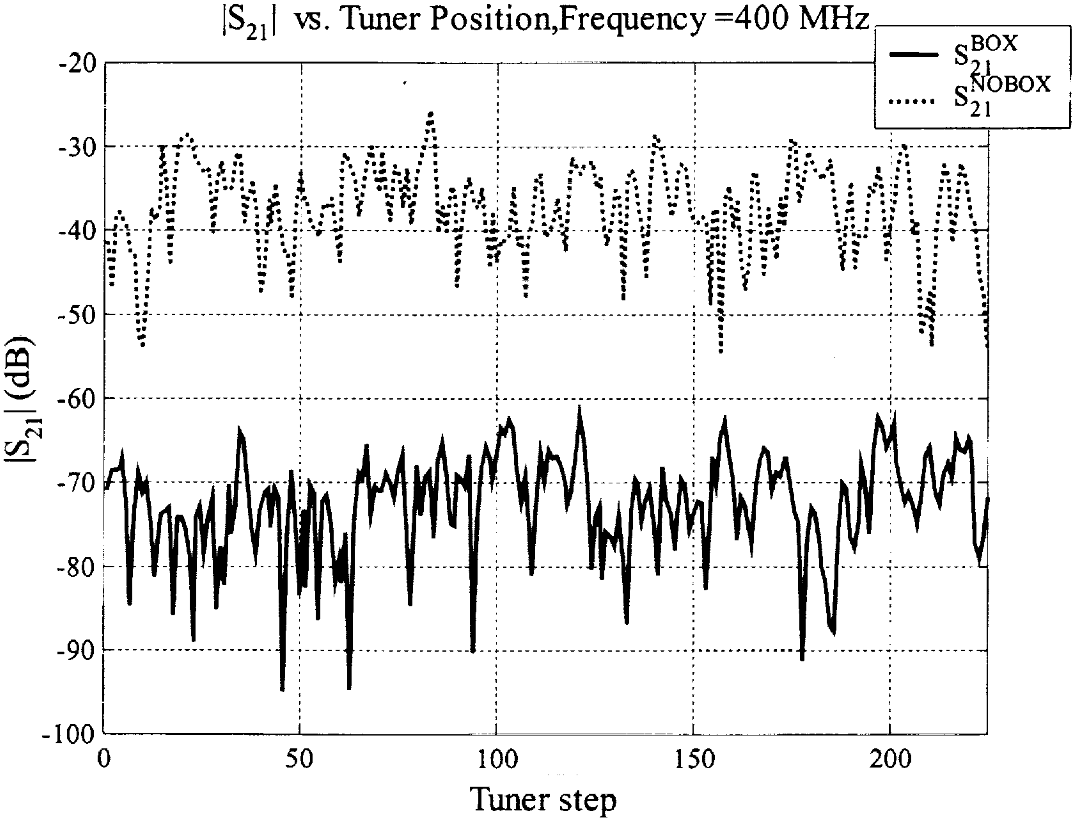

Figure 4.10. $|S_{21}|$ at 400 MHz for the shielded and unshielded configurations.

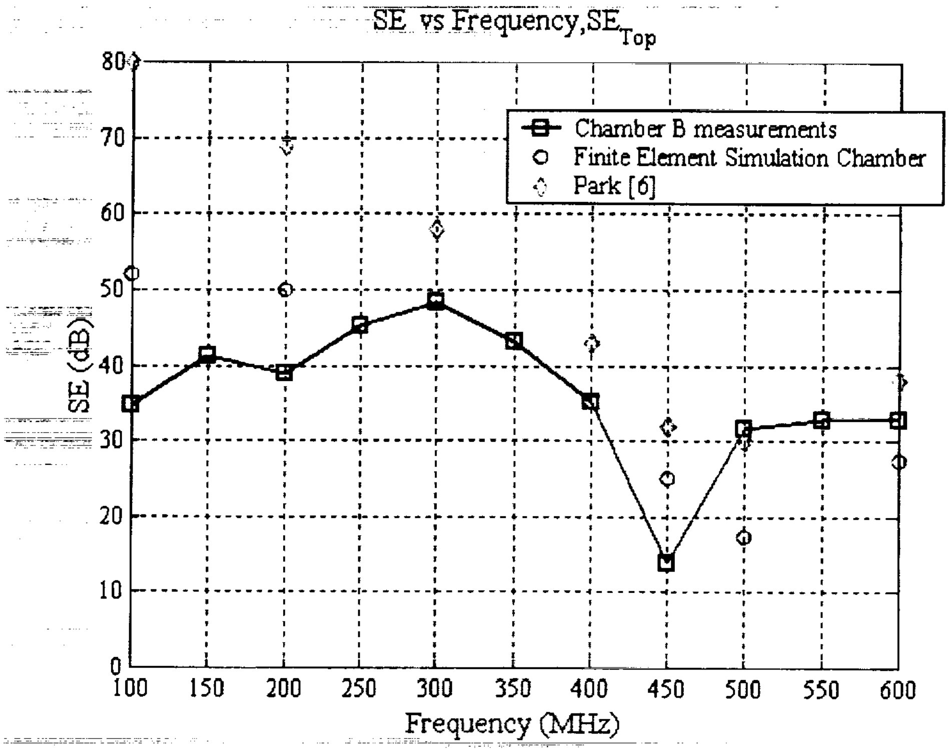

Figure 4.11. A comparison of reported [6], simulation chamber, and measured shielding effectiveness.

4.5 CONCLUSIONS

A two-dimensional finite element model for transverse magnetic (TM) solution inside a reverberation chamber has been presented. Tuner effects on the modal structure and the shielding effectiveness in a reverberating environment has been examined. The reverberating environment provides additional insight into the shielding properties in a statistical sense. The shielding effectiveness of the TM structure for aperture coupling for several frequencies in a simulated reverberation environment was presented and compared to published and measured results. These results point to the development of a statistical model of shielding effectiveness. This model will form a critical component to the overall mechanism of upset prediction in digital systems.

An example of an application of the notion of a probabilistic model for shielding effectiveness a problem of determining the probability of exceeding a particular voltage for a given input voltage. Consider the problem of determining the probability of having an electric field intensity of 1 V/m anywhere inside a cavity exposed at 1000 V/m. The shielding effectiveness was characterized earlier as a Normal random variable with mean of 35.3 dB and standard deviation of 10.5 dB at a frequency of 400 MHz. The probability of exceeding 1V/m for a 1000 V/m exposure corresponds to calculating the probability of having a shielding effectiveness less than 60 dB which is $F_{SE}(60) = 1 - Q\left(\frac{60-35.3}{10.5}\right) = 0.9906$. This calculation predicts a 99.06% probability of exceeding 1V/m for an exposure of 1000 V/m. If the threat level is reduced to 100 V/m the probability of exceeding 1 V/m reduces to 67.36 %.

4.6 REFERENCES

[1] G.J. Freyer, M.O. Hatfield, D.M. Johnson, and M.B. Slocum, "Characterization of the electromagnetic environment in aircraft cavities excited by internal and external sources," *AIAA/IEEE Digital Avionics Systems ConferenceProceedings*, October 1996.

[2] S.A. Scearce and C.F. Bunting, Statistical results for the UHF data from the NASA EME flight tests," *AIAA/IEEE Digital Avionics Systems ConferenceProceedings*, October 1998.

[3] Bunting, C.F., K.J. Moeller, C.J. Reddy, and S.A. Scearce, "A two-dimensional finite element analysis of reverberation chambers", *IEEE Trans. Electromag. Compat.*, vol. 41, pp. 280-289.

[4] D.L. Wu and D.C. Chang, "The effect of an electrically large stirrer in a mode-stirred chamber, " *IEEE Trans. on Electromag. Compat.*, vol. 31, no. 2, pp. 164-170, 1989.

[5] D.A. Hill, "Electronic mode stirring for reverberation chambers," *IEEE Trans. on Electromag. Compat.*, vol. 36, pp. 294-299, 1994.

[6] H. Y. Park and H. Y. Eom, "Electromagnetic penetration into 2-D multiple slotted rectangular cavity: TM wave," *IEEE Trans. on Antennas Propagat.*, vol. 48, pp. 331-333, 2000.